Obesogenic diet alters decidual differentiation and cell-cell communication in the mouse uterus

Burak Koksal[1,2], Christian J. Bellisimo[3-5], Patrycja A. Jazwiec[3-5], Deborah M. Sloboda[3-6], Alexander G. Beristain*[1,2]

[1] The British Columbia Children's Hospital Research Institute, Vancouver BC, Canada.
[2] Department of Obstetrics & Gynecology, The University of British Columbia, Vancouver BC, Canada.
[3] Department of Biochemistry and Biomedical Sciences, McMaster University, Hamilton, ON, Canada.
[4] Centre for Metabolism, Obesity, and Diabetes Research, McMaster University, Hamilton, ON, Canada
[5] Department of Obstetrics & Gynecology, McMaster University, Hamilton, ON, Canada
[6] Farncombe Family Digestive Health Research Institute, McMaster University, Hamilton, ON, Canada

*To whom correspondence should be addressed: Alexander G. Beristain, The British Columbia Children's Hospital Research Institute, The University of British Columbia, Vancouver, British Columbia, Canada. V5Z 4H4. Tel: (604) 875-3573; E-mail: aberista@mail.ubc.ca

Running Title: Obesity instructs changes in diverse endometrial cell types in early pregnancy

Keywords: Obesity, high-fat high sucrose, endometrium, pregnancy, stromal cell, immune cell, inflammation, single-cell RNA sequencing, decidualization, mouse

SUMMARY

Maternal obesity is associated with increased risk of infertility, implantation failure, miscarriage, and other pregnancy complications. While prior studies have linked obesity to uterine dysfunction and impaired endometrial biology, how obesity alters the cellular and molecular landscape of the early pregnant endometrium remains poorly understood. Here, we perform single-cell RNA sequencing of embryonic day 5.5 uterus from control and obesogenic mice to generate a cellular atlas of the early decidualizing endometrium. We identify obesity-associated transcriptional changes across multiple Endometrial Stromal Cell (ESC) states and innate immune populations, including uterine natural killer cells and macrophages. Computational modeling reveals that maternal obesity disrupts distinct routes of ESC differentiation during decidualization and leads to shifts in ESC-derived cues known to impact innate immune responses. These findings provide a comprehensive single-cell resource of the post-implantation mouse endometrium while simultaneously generating critical insight into how maternal obesity reprograms the maternal-fetal interface in early pregnancy.

INTRODUCTION

Early in pregnancy the uterus undergoes dramatic morphological and physiological remodeling to support embryo implantation and fetoplacental development. A central component of this transformation is decidualization, a process where endometrial stromal cells (ESCs) differentiate into specialized decidual stromal cells (DSCs) [1]. This cellular transformation is accompanied by coordinated changes in the uterine microenvironment, including the recruitment and functional reprogramming of immune cells [2,3], extensive vascular remodeling [4], and the establishment of a receptive decidual bed [5]. These processes are tightly regulated and temporally synchronized to facilitate implantation and to promote placental development. In humans, impaired or incomplete decidualization is associated with early pregnancy loss [6], implantation failure [7,8], and disorders of placentation such as preeclampsia [9,10], underscoring its importance not only for pregnancy success but also for the health of the mother and fetus.

Decidual transformation in the mouse is marked by the sequential formation of the primary and secondary decidual zones [11,12]. Formation of the primary decidual zone (PDZ) precedes the secondary decidual zone (SDZ), initiating between embryonic day (E)4.5-5.0 proximal to the implanted blastocyst at the anti-mesometrial pole. The mature PDZ is composed of tightly packed, non-mitotic decidual cells that form a barrier to immune cell infiltration and protect the early conceptus from oxidative stress [11]. As pregnancy progresses, a proliferative SDZ develops adjacent to the PDZ from E5.5 onward, expanding toward the mesometrial pole, ultimately contributing to the structural and functional decidua [11]. These spatially distinct regions play essential roles in modulating the local immune environment, regulating trophoblast invasion, and supporting the conceptus via histotrophic nutrition. While mice and humans differ in the cues initiating decidualization and the spatial distinctions of the PDZ and SDZ, the decidual compartments in the mouse share core physiological functions with the human decidua. Moreover, as in humans, impaired decidualization in mice is a primary driver of local immune dysregulation, placental dysfunction, and adverse reproductive outcomes [13].

Differentiation of ESCs into specialized PDZ and SDZ compartments is thought to be orchestrated by a complex interplay of signals derived from multiple maternal and embryonic cell types. These include uterine stromal, immune, epithelial, and endothelial cells, as well as blastocyst-derived trophoblasts, each contributing unique molecular signals that guide differentiation, modulate inflammation, and shape the local uterine environment [14–16]. While specific factors such as cytokines, growth factors, and extracellular matrix (ECM) components have been implicated in decidual remodeling [17–19], our understanding of how diverse cell types coordinate these processes, particularly in the immediate post-implantation period, remains incomplete.

Emerging evidence suggests that metabolic and immune processes profoundly influence decidualization [20,21]. Metabolic signaling additionally impacts uterine immune cells such as uterine natural killer (uNK) cells and macrophages (Mφ) that play key roles in tissue remodeling and vascular adaptation to pregnancy. Factors that

79 disrupt this relationship can impair decidualization and affect pregnancy success [22]. In this context, maternal
80 obesity, a chronic, low-grade inflammatory condition, has emerged as a factor that alters tissue metabolism and
81 immune cell function across multiple reproductive compartments [23–25]. Studies from both human cohorts and
82 animal models indicate that maternal obesity impairs endometrial function, reduces implantation rates, and is
83 linked to higher rates of miscarriage and pregnancy complications such as preeclampsia [26–29]. While work in IVF
84 clinical populations has underscored the contribution of obesity to endometrial-associated infertility [30], the
85 specific cellular and molecular mechanisms by which an obesogenic environment alters key endometrial processes
86 like decidualization during the earliest stages of pregnancy remain poorly understood.

87 To address this gap, we performed single-cell RNA sequencing (scRNA-seq) of implantation sites collected
88 at E5.5 from control chow and high fat/high sucrose (HFHS) diet-fed mice, a well characterized murine model of
89 maternal obesity[31,32]. This developmental timepoint captures early post-implantation events when decidual zones
90 are forming and extensive remodeling is initiated. This novel dataset offers a comprehensive transcriptional map
91 of uterine cell populations in healthy and obesogenic pregnancy and is available as a web-based resource (*Shiny*
92 *App*). Our analyses focus on *Hand2*$^{+}$ ESCs, a stromal cell type that initiates decidual transformation, and show that
93 an obesogenic diet disrupts gene signatures central to the control of inflammatory processes, cellular stress
94 responses, and pathways associated with decidualization. Applying single-cell trajectory tools, we show that
95 maternal obesity discretely impacts the development of the PDZ and SDZ. Lastly, we generate a cell-cell interactive
96 model showing how specific cell-cell interactions between endometrial stromal cell types and innate immune cells
97 in the early uterus are potentially altered by maternal obesity.

98 **RESULTS**

99 Establishment of E5.5 endometrial single-cell atlases of chow and obesogenic diet exposed mice

100 To determine how diverse endometrial cell types are affected by maternal exposure to an obesogenic
101 diet, a single-cell transcriptomic approach was applied (Fig. 1A). Briefly, C57BL/6J female mice were subjected to
102 either regular chow (Chow, n = 5) or HFHS (n = 5) diets for 12-15 weeks prior to timed-mating with Chow-fed
103 males. By four weeks of diet exposure, total bodyweight of HFHS mice was greater than Chow controls, and this
104 weight difference was maintained at conception (E0.5) and up to sacrifice at E5.5 (Fig. 1B; Fig. S1A). Along with an
105 overall increase in weight gain, HFHS exposure also led to increases in total body adiposity and peri-gonadal-
106 specific adiposity following ten weeks of diet and at embryonic day (E)5.5 (Fig. 1C; Fig. S1B). The latter increase in
107 gonadal adiposity is consistent with the effects of HFHS diet on metabolic disruption and low-grade inflammation
108 [33,34]. At E5.5, dams were euthanized and gravid uterine tissues were collected for downstream analysis. Pregnancy
109 was confirmed by the presence of visible uterine implantation swellings and via histology of the paired uterine
110 horn contralateral to that used for single-cell transcriptomics from each dam. Biological characteristics of
111 individual mice are summarized in Table S1.

112 Single-cell cDNA libraries were prepared and sequenced and following quality control and data pre-
113 processing, 72,349 endometrial cells from the combined Chow (33,556 cells) and HFHS (38,793 cells) groups were
114 integrated and plotted as a Uniform Manifold Approximation and Projection (UMAP) (Fig. 1E). Sequencing metrics
115 showed that percent mitochondrial RNA was not different between individual samples, however, numbers of
116 unique molecular identifiers (UMIs) and number of genes detected did show inter-sample variability, consistent
117 with sample differences in cell capture and sequencing depth (Fig. S1C). Within the combined object, 16 distinct
118 cell clusters were determined, including 6 immune (*Ptprc*$^+$) and 10 non-immune (*Ptprc*$^-$) cell clusters (Fig. 1E).
119 Leveraging both canonical cell-type markers [12,35,36] and the FindAllMarkers function in Seurat [37], specific cell
120 types/lineages were identified (Fig. 1E; Fig. S1D). The most prevalent cell types, representing over 70% of all cells
121 captured, were ESCs (S1-5; *Hoxa10*$^+$, *Hoxa11*$^+$, *Myh11*$^-$, *Mcam*$^-$), uNK cells (*Eomes*$^+$, *Nkg7*$^+$), and Mφs (*Adgre1*$^+$,
122 *Ms4a7*$^+$) (Fig. 1E; Fig. S1D). Additionally, two endothelial cell (Endo-1, -2; *Flt1*$^{+,}$ *CD34*$^+$), one epithelial cell (Epi;
123 *Epcam*$^+$), one mesothelial cell (Meso; *Upk3b*$^+$, *Lrrn4*$^+$)[38], one smooth muscle cell (SMC; *Acta2*$^+$, *Myh11*$^+$), two
124 classical dendritic cell (cDC-1, -2; *Zbtb46*$^+$), one T cell (T; *Cd3e*$^+$), and one innate lymphoid cell-like (ILC-like; *Eomes*$^+$,
125 *Cd209a*$^+$) types were also identified (Fig. 1E; Fig. S1D; Table S2). Within these subtypes, the Epi cluster contained
126 glandular epithelial (*Foxa2*$^+$, *Cxcl15*$^+$) and luminal epithelial cells (*Calb1*$^+$, *F3*$^+$) [39], while Endo-1 (*Flt1*$^+$, *Mcam*$^+$) and
127 Endo-2 (*Prox1*$^+$, *Mmrn1*$^+$) are likely vascular endothelial [40] and lymphatic endothelial cells[35], respectively (Fig. 1SD).
128 Four ESC clusters (S1-4) expressed *Hand2* transcripts, a marker indicative of ESCs committed to progesterone-
129 induced DSC differentiation (Fig. S1D) [41]. One *Hand2*$^-$ stromal cell population was also captured (S5) and this cell
130 state likely represents a population of deep stromal cells that do not participate in DSC transformation directly but

131 rather play roles in establishing endometrial structural support [42]. Notably, embryonic (epiblast) and
132 extraembryonic (trophoblast, primitive endoderm) cells of the conceptus were not captured, indicating that the
133 low proportion of this cellular material may preclude sufficient capture following single-cell workflow. Exposure
134 to HFHS diet did not result in significant differences in the proportion of distinct cell clusters or cell types (Fig. S1E),
135 though the proportion of endometrial Mφs trended toward being greater in frequency in HFHS mice (Fig. S1F).
136 Together, we used these data to create a near-comprehensive single-cell resource of the mouse uterus
137 immediately following blastocyst implantation in conditions modeling both healthy weight and maternal obesity
138 and can be explored using a user-friendly web-based interface (*Shiny App*).

139

140 **Obesogenic diet drives transcriptomic differences in select E5.5 endometrial cell types**

141 Following the initial characterization of this single-cell dataset, we next set out to examine if an obesogenic
142 diet affected transcriptional readouts in distinct endometrial cell types. Applying a Pearson's correlation
143 coefficient (PCC) analysis, we first investigated how maternal diet broadly affects endometrial cell gene signatures.
144 This was accomplished by combining all captured cells together followed by comparing the integrated gene
145 signatures of endometrial cells between Chow and HFHS groups. PCC analysis showed that the transcriptome of
146 HFHS endometrial cells was 94.3% similar to that of endometrial cells from Chow fed mice, suggesting that HFHS
147 challenge overall had a modest impact on endometrial cell gene expression (Fig. 2A). Next, a differential gene
148 expression (DGE) analysis was performed comparing the 13 distinct endometrial cell clusters in Chow and HFHS
149 diet groups; for these analyses *Hand2*$^+$ S1-4 stromal cell clusters were combined as one cluster. The greatest
150 number of differentially expressed genes (DEGs) were observed in ESCs (*Hand2*$^+$ and *Hand2*$^-$) and specific immune
151 cell types (i.e., uNK, Mφ, cDC2) (Fig. 2B; Table S3). Specifically, HFHS diet associated with 2063, 308, 307, 219, and
152 162 DEGs in *Hand2*$^+$ stromal, *Hand2*$^-$ stromal, uNK, Mϕ, and classic DC (cDC2) cells, respectively, with the majority
153 of DEGs showing increased levels in response to the HFHS diet (Fig. 2B). Markedly fewer numbers of DEGs were
154 identified in classic DCs (cDC1; 11 genes), ILC-like (10 genes), T (4 genes), lymphatic endothelial (Endo2; 4 genes),
155 vascular endothelial (Endo1; 3 genes), epithelial (Epi; 1 gene), and smooth muscle (SMC; 1 gene) cells (Fig. 2B). No
156 DEGs were identified in mesothelial cells between diet groups. Importantly, the number of DEGs per cell
157 type/cluster positively correlated with the number of cells per cluster (Fig. S2A), suggesting that in clusters
158 comprised of few cells, the actual impact of diet on gene expression is most likely underestimated. This is a
159 limitation of the single-cell RNA-seq platform and our approach to not enrich for low abundance cell types.

160 In decidualizing *Hand2*$^+$ ESCs of HFHS mice, top-ranked DEGs (Adj $P<0.05$; $Log_2FC>\pm0.4$) included genes
161 associated with lipid metabolism (*CD36*), inflammation/immune-related processes (*Galnt15*, *Tsc22d3*) [20,43], ECM
162 organization (*Adamts5*) [44], and decidual stromal cell functions (*Prlr*) [45,46] (Fig. 2C). Genes expressed at lower levels

163 in HFHS *Hand2*$^{+}$ cells associated with cell proliferation (*Plk2, Hist1h4d*) [47] and cellular stress (*GSTA3*) [48] (Fig. 2C). In
164 *Hand2*$^{-}$ stromal cells (i.e., deep ESCs), genes encoding ECM components show increased levels in HFHS mice (e.g.,
165 *Col11a1*, *Lama2*). Additionally, genes associated with vascular development (*Angptl4*, *Pdgfrl*) and pro-
166 inflammatory responses (*Igkc*) are also elevated in HFHS *Hand2*$^{-}$ stromal cells (Fig. 2C). Top genes downregulated
167 in HFHS *Hand2*- stromal cells include genes linked with cell proliferation (*Plk2, Hist1h4d*), ECM turnover (*Has1*),
168 and glucose metabolism (*Hk2*) (Fig. 2C). Like our observations in ESCs, genes showing greatest enrichment in uNK
169 cells and Mφs of HFHS mice included multiple ECM-encoding genes (*Col3a1*, *Dcn*, *Col1a1*, *Col1a2*) (Fig. 2C),
170 indicating the presence of fibrosis-like responses in uterine innate immune cell subsets. Uterine NK cells of HFHS
171 mice showed increases in inflammation-associated genes, with *Ifitm3* and *Ifi27l2a* as top ranked genes (Fig. 2C).
172 Only 3 coding genes showed decreased levels in expression in HFHS uNK cells, and these genes are associated with
173 calcium signaling (*Camk2b*), cell differentiation (*Sorcs2*), and glucose metabolism (*Hk3*) (Fig. 2C). In addition to
174 ECM-associated genes, top genes upregulated in Mφs included the cell membrane-associated metalloprotease
175 *MMP14* and *Cd33,* a gene encoding an immunoglobulin-like receptor important in regulating innate immune cell
176 functions (Fig. 2C).

177 Single-Cell Pathway Analysis [49] showed that HFHS diet resulted in the broad enrichment of pathways
178 central to interferon gamma signaling, hypoxia, cellular apoptosis and epithelial mesenchymal transition (EMT)
179 within multiple cell types (i.e., *Hand2*$^{+}$ stromal, *Hand2*$^{-}$ stromal, uNK, and Mφ) (Fig. 2D; Table S4). Enrichment of
180 the EMT process was most active in *Hand2*$^{-}$ ESCs, while enrichment of the interferon gamma response and other
181 pro-inflammatory responses were top-ranked pathways in uterine Mϕs (Fig. S2). Pathways enriched in *Hand2*$^{+/-}$
182 stromal cells and Mϕs of control Chow fed mice included Myc, mTOR signaling, and E2F-directed DNA replication
183 (Fig. 2D), while uNK cells showed specific enrichment of the unfolded protein response pathway (Fig. S2B).
184 Notably, while these endometrium-residing cell types showed enrichment of many of the same gene pathways,
185 the vast majority of DEGs were unique to each cell type with only 8 DEGs shared between *Hand2*$^{-/+}$ stromal cells,
186 uNK cells, and Mϕs (Fig. 2E), suggesting that HFHS diet leads to distinct cell-type gene signatures that converge
187 into conserved gene pathways. Together, HFHS-directed transcriptomic differences in E5.5 endometrial cell types
188 suggest that maternal obesity affects multiple cell types, predominately immune and structural/functional stromal
189 cells important in endometrial biology and pregnancy.

190

191 **Obesogenic diet disrupts gene pathways central to inflammation and cell stress in *Hand2*$^{+}$ stromal cells**

192 Because the obesogenic diet led to more transcriptomic differences in *Hand2*$^{+}$ stromal cells than in other
193 endometrial cell types, we next set out to more closely examine the effect of HFHS diet on this stromal cell
194 population that is central to DSC transformation. To do this, *Hand2*$^{+}$ cells were subset from the main single-cell

195 object and re-clustered, resulting in five new cell clusters (Fig. 3A). These re-clustered *Hand2*$^{+}$ cells segregated into
196 1) undifferentiated stromal cells (UnStr; *Vim*^{hi}, *Snai2*^{hi}, *Igfbp5*^{hi}), 2) primary decidual zone cells (PDZ1-2; *H19*$^{+}$,
197 *Dio3*$^{+}$, *Bmp2*$^{+}$), and 3) secondary decidual zone cells (SDZ1-2; *Apoe*^{hi}, *Igfbp3*^{hi}, *Foxp2*$^{+}$) (Fig. 3A; Fig S3A). The identity
198 of these cell states was determined using previously annotated gene signatures of distinct *Hand2*$^{+}$ cell types [12,50,51]
199 (Fig. S3A; Table S5). While the proportions of UnStr cells captured were identical between Chow and HFHS groups,
200 PDZ cell proportions from Chow mice were slightly greater than those found in HFHS mice (~24% Chow vs 20%
201 HFHS) (Fig. S3B). This contrasted with SDZ cell proportions that showed a moderate increase in HFHS (45%) over
202 Chow (41%) (Fig. S3B). These potential differences in *Hand2*$^{+}$ stromal cell type frequencies suggest that obesogenic
203 diet may affect decidualization in subtle ways impacting both the initial PDZ response as well as the formation of
204 the functional decidua.

205 To examine the effect of HFHS diet on transcriptomic readouts in *Hand2*$^{+}$ cells, we next performed a DGE
206 analysis comparing the five *Hand2*$^{+}$ cell states between Chow and HFHS diet groups. While DEGs were identified
207 in all *Hand2*$^{+}$ cells, the SDZ1 and SDZ2 clusters showed the greatest numbers of DEGs; most genes (SDZ1: 867 of
208 1276; SDZ2: 1138 of 1581) showing increased levels in response to HFHS challenge (Fig. 3B; Table S6). In UnStr,
209 PDZ2, and SDZ2 stromal cells, 48 DEGs were common to all three cell states, where many of these genes associated
210 with immuno-regulatory functions, including complement activation and antigen presentation (*Cfh*, *Cd74*, *H2-Aa*,
211 *H2-Eb1*, *Ppp3ca*) (Fig. 3C). The majority of DEGs showed cell-state specificity in expression but nonetheless
212 converged into processes common in all three cell types like inflammation and immune function (Fig. 3C). Among
213 top DEGs in UnStr cells (defined as Adj $P<0.05$; $Log_2FC>\pm0.4$), HFHS diet led to increased levels of the complement
214 pathway transcript *C3* and the Krüppel-like transcription factors *Klf5* and *Klf15*, while levels of the chemokine
215 *Cxcl5*, the cell cycle-associated serine/threonine kinase *Plk2*, and the transcription factor *Scx* showed reductions
216 in HFHS (Fig. 3D; Table S6). In the PDZ-1 state in response to HFHS diet, top DEGs showing increased levels include
217 the EMT-regulator *Unc13c* [52], the growth factor receptor *Kit*, the transcription factor *Gata3*, and the morphogen
218 *Bmp2*; the latter playing an important role in promoting decidualization [53] (Fig. 3D; Table S6). Conversely, top
219 genes showing elevated expression levels in Chow control PDZ1 cells include the glycine acetyltransferase *Gcat*,
220 and nucleosome-associated transcripts *Hist1h1e* and *Hist1h4d* (Fig. 3D). In the PDZ2 state, genes encoding AP1
221 transcription factors were elevated in HFHS, including *Fos* and *Fosb*, as was the transcription factor *Snai2* and
222 *Unc13c* (Fig. 3D). Like the PDZ1 state, multiple genes encoding nucleosome-associated histone proteins were
223 expressed at higher levels in Chow PDZ2 cells, including *Hist1h2bj*, *Hist1h2ai*, *Hist1h2ac*, *Hist1h3* and *Hist1h3g*,
224 suggesting these cells are actively proliferating or undergoing epigenetic reprogramming (Fig. 3D). In HFHS SDZ1
225 cells, top genes included *Prlr* (encoding the prolactin receptor), the Jak/Stat pathway inhibitor *Socs2*, the
226 aggrecanase *Adamts5*, and *Chodl,* a transcript encoding a lectin-binding receptor with unknown function [54] (Fig.
227 3D). Top genes enriched in control Chow SDZ1 cells included the cell adhesion molecule *Thy1*, the norepinephrine

228 transporter Slc6a2 and *Dctpp1*, encoding DCTP pyrophosphatase 1 (Fig. 3D). In the SDZ2 cell state, top ranked
229 genes elevated in HFHS included the ligand *Kitl* (encoding stem cell factor), pro-inflammatory *Tnfaip2*, the Wnt
230 inhibitor *Dkk2*, and growth factor *Fgf10*, whereas top genes expressed in Chow SDZ2 cells included the morphogen
231 *Bmp7*, nitric oxide synthase *Nos1*, and *Ptpro* encoding a receptor-tethered protein tyrosine phosphatase (Fig. 3D).
232 *In situ* hybridization (ISH) was performed to validate diet-associated differences in two of the highest ranked DEGs,
233 *Nos1* and *Unc13c in* SDZ and PDZ stromal cell types (Fig. 3E; Fig. 3SB), respectively. ISH confirmed localization of
234 *Nos1* and *Unc13c* to *Hand2*$^+$ endometrial stromal cells, with *Nos1* showing specificity to the SDZ and *Unc13c* to
235 the PDZ (Fig. 3F; Fig. S3C). Qualitatively, ISH signals of *Nos1* and *Unc13c* appeared lower and higher, respectively,
236 within endometrial regions of HFHS mice, supporting our scRNA-seq findings (Fig. 3F).

237 Lastly, Single-Cell Pathway Analysis was performed to further understand the impact of HFHS diet on
238 *Hand2*$^+$ ESCs. Like our findings in our single-cell object representing diverse endometrial cell types (Fig. 2E), HFHS
239 challenge led to the enrichment of conserved pathways across all *Hand2*$^+$ cell states, including response to
240 hypoxia, the complement cascade, EMT, and IFN-γ signaling (Fig. 3G; Fig S3D; Table S7). In PDZ and SDZ cell types,
241 oxidative phosphorylation, reactive oxygen species, mTor signaling, and Myc signaling pathways were dampened
242 in response to the HFHS diet (Fig. 3G; Fig S3D). HFHS diet also led to the enrichment of other stress- and
243 inflammatory-related pathways in *Hand2*$^+$ cells, including TNF signalling, coagulation, UV response, apoptosis, and
244 DNA repair (Table S7), suggesting that exposure to an obesogenic diet establishes an *in utero* environment that
245 imparts conserved inflammatory, cell stress, and metabolic responses in *Hand2*$^+$ stromal cell types of the
246 endometrium.
247

248 Obesogenic diet alters PDZ and SDZ differentiation kinetics

249 To understand how maternal obesity affects the early stages of PDZ and SDZ formation, integrated
250 datasets of Chow and HFHS mice, subset for *Hand2*$^+$ ESCs, were subjected to single-cell trajectory analysis.
251 Applying Monocle2 [55] pseudotime ordering to *Hand2*$^+$ cells, a start point enriched in UnStr cells was identified that
252 bifurcated along two distinct pathways culminating in either PDZ2 or SDZ2 cell states (Fig. 4A; Fig. S4A). Along each
253 bifurcated trajectory, *Hand2*$^+$ cells progressed first into either PDZ1 or SDZ1 cell states before terminating into
254 either PDZ2 or SDZ2 endpoint states (Fig.4A). Midway through the SDZ trajectory, an additional small branch was
255 observed that showed enrichment of cells expressing senescence-associated genes (Fig. 4A; Fig S4A). These cells
256 are likely senescent stromal fibroblasts and are a byproduct of decidualization [56]. This novel differentiation path,
257 that PDZ and SDZ cells emerge via distinct routes of differentiation from a common endometrial stromal cell
258 progenitor, is to our knowledge a new observation not previously reported. To more robustly explore this
259 differentiation process, we applied Monocle3 [57], another pseudotime ordering tool and showed that similar to
260 Monocle2, UnStr cells localize to the trajectory origin and progress into two major trajectory arms that give rise

261 to either PDZ or SDZ cell states (Fig. S4B). Rendering the Monocle3 trajectory into 3D clearly shows the two distinct
262 arms of *Hand2*$^{+}$ stromal cell differentiation (Figs S4C; S4D). Altogether, these analyses suggest that PDZ and SDZ
263 are developmentally and functionally distinct uterine compartments that can be resolved transcriptionally as early
264 as E5.5 in the mouse endometrium.

265 We then set out to determine whether this bifurcation is vulnerable to maternal diet. Subsetting *Hand2*$^{+}$
266 cells based on diet and re-applying Monocle2 ordering shows that both Chow and HFHS cells follow a similar
267 bifurcated route of differentiation into PDZ and SDZ cell states (Fig. 4B). However, in the HFHS trajectory, UnStr
268 cells progress along a more elongated path before bifurcating into PDZ and SDZ arms (Fig. 4B). Additionally, the
269 putative senescent stromal fibroblast branch along the SDZ route in HFHS cells occurred earlier in pseudotime in
270 HFHS cells, suggesting that DSC differentiation may be accelerated in this obesogenic model. This interpretation
271 is further supported by the fact that SDZ2 cells of HFHS mice progressed empirically further in pseudotime than
272 SDZ2 cells of Chow mice (Fig. 4B). Correlating the expression of known genes specific to undifferentiated (*Fmod,*
273 *Vim, Sfrp4)*, PDZ (*Dio3*, *Id1*, *Ran*), and SDZ (*Mef2a, Rb1cc1, Map2*) differentiation states with the pseudotime
274 trajectory confirmed the accuracy of the pseudotime modeling (Fig. 4C). When we correlated *Hand2*$^{+}$ stromal cell
275 trajectories with 38 top-ranking DEGs between Chow and HFHS conditions with branch-specific expression
276 patterns, they showed subtle differences not only in gene level intensity but also at specific points along
277 pseudotime (Fig. 4C). For example, in Chow mice multiple genes (e.g., *Actb, Igfbp2, Romo1*) increased in expression
278 earlier along the PDZ trajectory. This contrasted with the SDZ trajectory, where HFHS cells showed increased levels
279 of most DEGs (e.g., *Il13ra2, Foxp1, Kitl*) earlier along pseudotime. These findings suggest that decidualization
280 kinetics are different in *Hand2*$^{+}$ Chow and HFHS ESCs.

281 To more thoroughly evaluate how specific *Hand2*$^{+}$ stromal cell states change across pseudotime, we
282 mapped cells onto a Slingshot-inferred trajectory [58], which, consistent with our models generated using Monocle2
283 and Monocle3, identified a bifurcated differentiation pathway originating from UnStr cells and diverging toward
284 either a PDZ or SDZ fate (Fig. S4E). Density-based analysis of cell distributions along pseudotime revealed that at
285 E5.5 the HFHS uterus exhibits a modest but statistically significant enrichment of UnStr cells early in pseudotime
286 and a corresponding depletion of terminally differentiated PDZ cells (Fig. 4D). In contrast, SDZ endpoint cells were
287 slightly more enriched in the HFHS condition (Fig. 4D), suggesting that maternal obesity may bias lineage allocation
288 or alter maturation kinetics across these two discrete decidualization pathways. Our findings suggest that
289 maternal obesity may impair formation of the PDZ and accelerate formation of the SDZ. To assess this latter point,
290 we examined the distribution and signal intensity of *Hand2* transcript, a gene under positive regulation of the
291 progesterone receptor and a marker of decidualization (Fig. 4E). *Hand2* positivity tended to be more profusely
292 distributed in the E5.5 endometrium of HFHS mice, suggesting that decidualization may be increased or
293 accelerated compared to Chow mice, although this difference did not reach statistical significance (Fig. 4E; Fig.

294 4F). However, the number of *Hand2* transcripts in cells within the SDZ was greater in HFHS mice than in Chow
295 mice, a finding that supports our single-cell modeling suggesting that SDZ development is enhanced in obesogenic
296 conditions (Fig. 4F). Focussing on the PDZ, we next examined the effect of HFHS diet on states of PDZ maturation
297 by measuring cell density and size, since the mature PDZ is composed of densely packed cells arranged around the
298 perimeter of the implantation crypt. In Chow mice, a strong, dense *Hand2* signal was detected in the PDZ while in
299 HFHS mice, *Hand2* positive cells were spatially more diffuse within the PDZ region (Fig. 4E). These qualitative
300 assessments correlated with an increase in cell size and a corresponding decrease in number of cells in the PDZ
301 region in Chow mice compared to HFHS mice, suggesting that PDZ establishment is impaired in obesogenic mice
302 (Fig. 4F). Together our single-cell transcriptomic data and observational histology suggest that maternal
303 obesogenic condition likely modify PDZ development and accelerated the formation of the SDZ at E5.5 in mice.
304

305 **Maternal obesity impacts *Hand2*$^{+}$ ESC-directed activities of resident innate immune cells**

306 Our observation that an obesogenic diet alters immune-modulating and inflammation-related gene
307 pathways in ESCs led us to investigate how these changes might influence intercellular communication with key
308 immune cell populations in the E5.5 endometrium. To address this, we applied CellChat analysis [59] to our single-
309 cell transcriptomic data to model putative ligand-receptor interactions among relevant cell types. We focused our
310 analysis on *Hand2*$^{+}$ ESCs, uNK cells, and Mφs, the three most abundant populations captured in our single-cell
311 dataset and the principal cellular mediators of stromal-immune crosstalk at this developmental stage. We first
312 determined relative changes in both the number and strength of predicted cell-cell interactions across
313 experimental groups (Fig. 5A; 5B; Fig, 5SA). HFHS diet increased the number of signaling interactions directed
314 towards Mφ and SDZ1 cells (Fig. 5A). Conversely, signaling interactions originating from or directed towards PDZ1,
315 PDZ2, and SDZ2 stromal cells were reduced in HFHS implantation sites (Fig. 5A). When evaluating interaction
316 strength, PDZ states in both Chow and HFHS conditions were shown to be the strongest producers of ligands
317 whereas uNK and Mφ immune cell populations showed the greatest receiver potential suggesting the PDZ at E5.5
318 serves as the primary source of immune-modulating factors (Fig. S5A). Notably, HFHS diet led to marked increases
319 in ESC-directed cell-cell interaction strengths toward uNK and Mφ populations, suggesting an enhancement of
320 immunoregulatory signaling under obesogenic conditions (Fig. 5A). HFHS exposure was predicted to lead to
321 marked increases in uNK-regulating ligands by SDZ2 cells, with high probability of predicted interactions between
322 uNK-expressed nucleolin receptor (*Ncl*) and SDZ2-expressed midkine (*Mdk*) and pleiotrophin (*Ptn*) ligands (Fig.
323 S5B). Additionally, UnStr and PDZ stromal cells from HFHS mice showed marked increases in ligand-directed
324 interactions with Mϕs, driven largely by elevated macrophage migration inhibitory factor (*Mif*) and amyloid
325 precursor protein (*App*) ligand expression in UnStr and PDZ cell types with increases in *Cd74*, *Cxcr4*, and *Trem2*
326 expression in Mφs (Fig. S5C).

327 To identify pathways disproportionately altered by HFHS diet, we next ranked signaling pathways based
328 on their relative contributions to overall cell-cell communication under each condition (Fig. 5B; Table S8). Multiple
329 pathways were enriched in HFHS, including the immunomodulatory and inflammation-regulating Galectin and
330 Cxcl-related chemokine pathways and the cell differentiation-associated Fibronectin Leucine-Rich
331 Transmembrane protein (FLRT), TGFβ, and UNC5 (netrin receptor) pathways. In contrast, fibroblast growth factor
332 (FGF), non-canonical (nc)Wnt, and desmosterol signaling were significantly diminished within *Hand2*$^{+}$ stromal, uNK
333 and Mφ cell types (Fig. 5B). Notably, desmosterol signaling, a pathway important in cholesterol biosynthesis and
334 immune cell modulation [60], showed a substantial reduction in PDZ cells of HFHS mice (Fig. 5C), suggesting possible
335 diet-dependent suppression of sterol-mediated signaling pathways and desmosterol-directed immune cell
336 dampening in PDZ-stromal communication. To this end, *Dhcr7*, encoding dehydrocholesterol reductase, an
337 enzyme important in cholesterol synthesis, showed decreased levels in HFHS PDZ1 cells, while levels of the
338 transcript encoding Liver X receptor (*Nr1h2*) that binds to and propagates the desmosterol signal, was damped in
339 SDZ2 stromal cells and Mφs (Fig. 5D). In contrast, Galectin signaling, important in driving immunosuppressive
340 signals and shown to impede vascular remodelling in the uterus [61], was among the most strongly enriched
341 pathways in HFHS mice, and this was driven primarily by increased paracrine and autocrine-mediated activity from
342 Mφs (Fig. 5E). In these respects, Galectin-9 transcripts (i.e., *Lgals9*) were increased in HFHS Mϕs, while various
343 Galectin-9 receptor transcripts (*Ptprc, Ighm, Cd44, P4hb, Havcr2*) showed increased levels in all *Hand2+* stromal
344 cell types, uNK, and Mφs, the latter pointing to the increase in Galectin autocrine signaling (Fig. 5F).
345 Together, these findings indicate that HFHS diet exposure reshapes the maternal endometrial
346 communication network during early pregnancy, reducing stromal-derived sterol signaling while enhancing
347 immune-dominated interactions and glycan-mediated pathways between distinct states of *Hand2*$^{+}$ endometrial
348 stromal cells, uNK cells, and decidual Mφs.
349
350

351 **DISCUSSION**

352 Despite growing evidence that maternal obesity impairs endometrial receptivity and decidualization, the
353 cellular mechanisms underlying these effects remain poorly understood. In particular, the impact of obesogenic
354 environments on the post-implantation endometrium has not been examined at single-cell resolution. In this
355 study, we used single-cell RNA sequencing to generate a comprehensive cellular and transcriptomic map of the
356 early decidualizing endometrium in mice fed a control or obesogenic diet. We have also created a publicly
357 accessible web-based resource (*Shiny App*) of the early endometrial cell landscape. We show that maternal HFHS
358 diet leads to enhanced pro-inflammatory and cell stress responses in both ESCs and uterine-resident innate
359 immune cells. Using both computational modeling and *in situ* analyses, we demonstrate that an obesogenic diet
360 leads to changes in the formation of DSCs, as evidenced by altered expression of genes along PDZ and SDZ
361 differentiation trajectories and characterization of PDZ structure. We also show that key cell-cell interactions
362 between *Hand2*$^{+}$ ESCs, uNK cells, and Mφs are disrupted under HFHS conditions, particularly in signaling pathways
363 regulating immune cell activity and tolerance. Together, these findings provide novel insight into how obesity
364 perturbs the cellular architecture and signaling landscape of the uterus during the earliest stages of pregnancy.

365 Previous studies have consistently reported that maternal obesity is associated with impaired endometrial
366 function, both in natural [28,62] and assisted conception contexts [63]. Work from IVF cohorts shows that obesity
367 negatively impacts endometrial receptivity and embryo implantation rates, independent of oocyte or embryo
368 quality [27,30]. Transcriptomic analyses of endometrial biopsies from obese women have further identified
369 widespread dysregulation of genes involved in inflammation, oxidative stress, and ECM remodeling [64].
370 Complementary studies in rodent models have echoed these findings, with RNA-sequencnig of whole uterine
371 tissue and bulk cell-sorted populations revealing obesity-induced transcriptional shifts in epithelial and stromal
372 compartments, including enrichment of immune-related and metabolic pathways [65]. However, these prior studies
373 lacked single-cell resolution and were limited to either the pre-implantation period or non-pregnant states, making
374 it difficult to capture pregnancy specific responses like decidualization. Our work addresses this gap by providing
375 the first single-cell atlas of the mouse post-implantation endometrium in the context of maternal obesity.

376 The PDZ is the first region of the endometrium to undergo stromal cell differentiation following blastocyst
377 attachment, forming a specialized niche critical for protecting the embryo during early pregnancy [66]. This process
378 is initiated by a convergence of hormonal cues and embryo-derived signals that promote the transformation of
379 ESCs into *Hand2*$^{+}$ DSCs. Notably, we provide evidence using cell trajectory-based inference that PDZ formation is
380 a distinct developmental process to that of SDZ transformation. To our knowledge, distinct DSC differentiation
381 pathways originating from common stromal cell decidual cell precursors has not been previously reported. In light
382 of these novel findings, future work should investigate specific regulators of these disparate developmental

383 pathways as the PDZ and SDZ regions play specialized and distinct roles in embryo development and pregnancy
384 health.

385 *Hand2* is a key transcriptional regulator of this differentiation process and is expressed in high levels in
386 cells of the early PDZ [67]. In our study, we used single-cell trajectory analyses to show that the formation of the PDZ
387 is blunted in HFHS mice, where *in situ* analyses examining *Hand2* distribution and expression show that the
388 cellularity and compactness of the PDZ region is altered in HFHS diet-fed mice. These findings suggest that PDZ
389 formation may be impaired or poorly synchronized in the context of maternal obesity. Since our single-cell data
390 revealed that SDZ differentiation may be accelerated in HFHS-fed mice, this raises the possibility that premature
391 emergence of SDZ-like cells disrupts the spatial and temporal fidelity of PDZ formation. However, our histological
392 data suggest this SDZ feature is modest at best. Nonetheless, the consequences of PDZ disorganization could be
393 important as it not only acts as a physical barrier shielding the embryo but also plays a critical immunomodulatory
394 role [68], shaping the local uterine immune environment to support embryo tolerance and implantation. If PDZ
395 formation is weakened or spatially dysregulated, ESCs may fail to establish the proper stromal-immune signaling
396 gradients necessary to restrain inflammatory immune activity in the immediate peri-embryonic space. This
397 possibility is supported by our identification of altered expression of immune-regulatory transcripts such
398 as multiple AP1 transcription factor-encoding transcripts and multiple interferon-response genes (ISGs) within the
399 decidualizing stroma, as well as disrupted ligand-receptor interactions between *Hand2*$^{+}$ PDZ cells, uNK cells, and
400 decidual macrophages in HFHS mice. Together, these findings suggest that maternal obesity perturbs early
401 decidual organization in a way that may compromise the immunological integrity of the maternal–fetal interface.

402 In addition to revealing shifts in stromal differentiation dynamics, our single-cell communication analyses
403 identified diet-induced disruptions in specific paracrine signaling pathways between ESCs and uterine immune
404 cells. Notably, CellChat analyses showed that desmosterol signaling, originating primarily from PDZ stromal
405 subsets, was markedly reduced in HFHS-exposed mice. Desmosterol, a cholesterol biosynthesis intermediate, acts
406 as a ligand for liver X receptors (LXRs), which regulate inflammatory responses in macrophages and other immune
407 cells [60]. Its reduction may therefore contribute to a pro-inflammatory shift in the local decidual environment. In
408 contrast, Galectin signaling, particularly through Galectin-9 (*Lgals9*), was enriched under HFHS conditions.
409 Galectin-9 is a glycan-binding protein with complex immunoregulatory roles, including modulation of T cell
410 exhaustion, NK cell cytotoxicity, and Mφ polarization [69,70]. Enhanced Galectin-9 signaling from decidualizing ESCs
411 toward uNK and macrophage populations may reflect a compensatory or dysregulated attempt to restrain
412 inflammation in the context of maternal metabolic stress. Together, these HFHS-induced ligand-receptor
413 differences highlight how maternal obesity reshapes the immune-regulatory signaling landscape of the decidua,
414 potentially altering the balance between pro- and anti-inflammatory cues in its early formation.

415 While maternal obesity is a well-established risk factor for adverse pregnancy outcomes in humans, our
416 HFHS mouse model does not recapitulate all aspects of this clinical phenotype. Although HFHS-fed females exhibit
417 reduced fertility [71], requiring more mating attempts to establish pregnancy, the number of implantation sites and
418 fetal and placental weights at E17.5 are not significantly different from Chow-fed controls [72]. These observations
419 are consistent with some, but not all reports in the literature, where variability in diet composition, strain
420 background, and environmental factors likely contribute to divergent outcomes. We deliberately chose a standard
421 chow diet as a control, rather than a purified, calorie-matched control diet, because this better recapitulates the
422 human context. While nutrient-matched control diets are optimal for isolating the effects of specific
423 macronutrients, they do not reflect the broader dietary shifts that occur in human populations consuming high-
424 fat, energy-dense foods that results in increased adiposity. In humans, high-fat diets are rarely consumed in
425 isolation but are accompanied by changes in micronutrient density, fiber type, and food processing. By comparing
426 a high-fat diet to standard chow, we model the combined nutritional changes typical of real-world diets,
427 prioritizing translational relevance over strict nutrient matching. Despite the absence of gross pregnancy defects,
428 our study reveals substantial obesity-related alterations in differentiation dynamics and intercellular signaling
429 within the peri-implantation endometrium. These findings raise the possibility that maternal obesity may induce
430 subtle or latent disruptions in uterine biology that are not sufficient to compromise fetal growth under controlled
431 laboratory conditions but could render pregnancies more vulnerable to additional environmental or physiological
432 stressors. Indeed, our prior work has shown that maternal HFHS exposure impairs spiral artery remodeling at mid-
433 gestation (E10.5), although these defects normalize by E17.5 [73]. Together, these findings suggest that the effects
434 of maternal obesity may be developmentally transient or context-dependent, with compensatory mechanisms
435 buffering the uterine environment in the absence of secondary insults. Future studies incorporating additional
436 stressors, such as infection, social stress, or hypoxia, may help reveal the full extent to which an obesogenic uterine
437 environment sensitizes pregnancies to failure or dysfunction, providing a more faithful parallel to the complex and
438 multifactorial nature of human pregnancy complications.

439 **Limitations of the study**

440 This study uses a mouse model of diet-induced obesity, which, while valuable for dissecting mechanistic
441 pathways, does not fully recapitulate the complexity of human obesity, including its metabolic, hormonal, and
442 inflammatory diversity. Additionally, our use of single-cell RNA sequencing is limited by biases in cell capture and
443 detection sensitivity. Rare and fragile cell populations may be underrepresented, affecting both cluster
444 resolution and statistical power in differential expression analyses. Moreover, single-cell transcriptomics lacks
445 spatial context, which is a notable limitation in the uterus—a highly structured and spatially dynamic tissue.
446

ACKNOWLEDGEMENTS

We thank Dr. M Shannon for his help with *in situ* hybridization. We thank members of the Beristain laboratory, specifically Matthew Shannon, Gina McNeill, and Victoria Leonard, for their critical reading and feedback of this manuscript. We additionally thank the computational resources provided by the Advanced Research Computing Team, University of British Columbia.

Funding: This work was supported by a Canadian Institutes of Health Research Project Grant (202109PAV-468535-CA2) (to AGB); and a Canadian Institutes of Health Research Project Grant (PJT175293) (to DMS). CJB was supported by a doctoral Canada Graduate Scholarship (CGS-D) awarded by the Canadian Institutes of Health Research.

AUTHOR CONTRIBUTIONS

Conceptualization: A.G.B., C.J.B., D.M.S.; Methodology: B.K., C.J.B., P.A.J., D.M.S., A.G.B.; Formal analysis: bioinformatic – B.K., animal work and benchwork – B.K., P.A.J., C.J.B.; Resources: A.G.B., D.M.S.; Writing: original draft – B.K., A.G.B.; review & editing – B.K., C.J.B., D.M.S., A.G.B.; Supervision: A.G.B., D.M.S.; project administration: A.G.B. Funding acquisition: A.G.B., D.M.S.

DECLARATION OF INTERESTS

The authors declare that no competing interests exist.

467 **MAIN FIGURE TITLES AND LEGENDS**

468 **Figure 1: Characterization of obesogenic mouse model and establishment of E5.5 uterine cell atlas**

469 (**A**) Schematic overview of the experimental design. Female C57BL/6J mice were fed a control chow or a high-fat
470 high-sucrose (HFHS) diet for 12 weeks prior to mating (n = 5 per diet group). Uterine horns with intact implantation
471 sites harvested at embryonic day 5.5 (E5.5) were used for histology or cell preparations for single-cell RNA
472 sequencing. (**B**) Weekly body weight measurements over 12 weeks of dietary intervention. Statistical analyses
473 between groups were performed using repeated measures ANOVA with post-hoc Bonferroni-corrected pairwise
474 comparisons; significance: *$p < 0.05$. Data shown as mean ± standard deviation; weights of individual dams are
475 depicted. GD = gestational day. (**C**) Preconception adiposity relative to bodyweight (%) at 0 and 10 weeks of diet.
476 Two-way repeated measures ANOVA was performed; significance: *$p < 0.05$. (**D**) Representative brightfield image
477 of an H&E stained E5.5 implantation site; scale bar = 500 μm. Em: embryo; PDZ: Primary Decidual Zone; SDZ:
478 Secondary Decidual Zone. (**E**) UMAP plot of 72,349 cells from E5.5 implantation sites of Chow (n=5; 33,556 cells)
479 and HFHS (n=5; 38,793 cells) mice. Cell state clusters are indicated as numbers on the UMAP: Endometrial stromal
480 cell clusters (ESC) 1-5 (S1-S5); uterine natural killer cell (uNK); T cell (T); innate lymphoid cell-like (ILC-like);
481 macrophage (Mφ); conventional dendritic cell 1 & 2 (cDC1, cDC2); endothelial cell 1 & 2 (Endo1, Endo2); epithelial
482 cell (Epi); mesothelial cell (Meso), smooth muscle cell (SMC). Solid line outlines clusters specific to ESC states
483 whereas hashed line highlights clusters specific to immune cells.

484

Figure 1

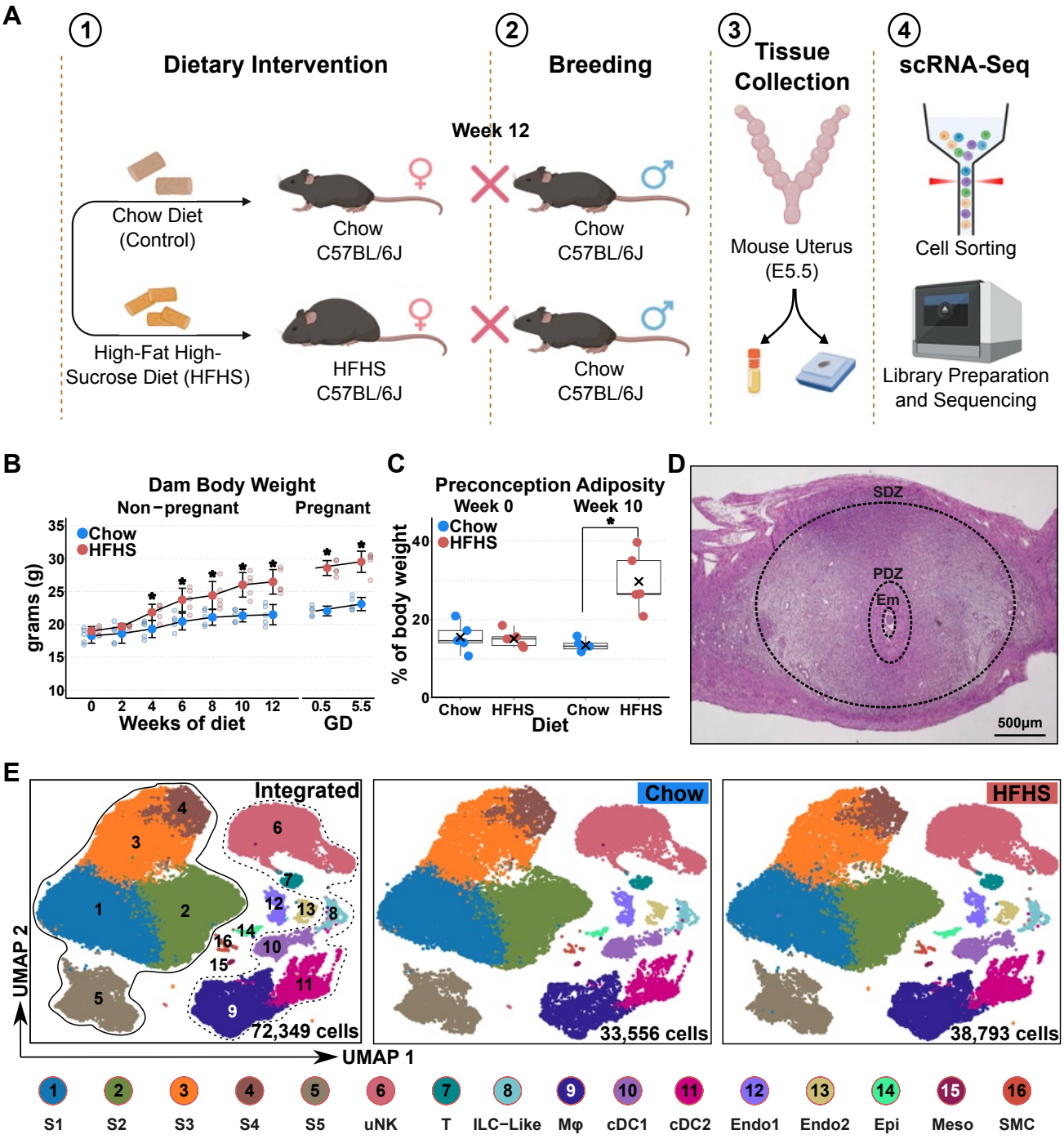
A
1
Dietary Intervention
2
Breeding
3
Tissue Collection
4
scRNA-Seq
Week 12
Chow Diet (Control)
Chow C57BL/6J
Chow C57BL/6J
High-Fat High-Sucrose Diet (HFHS)
HFHS C57BL/6J
Chow C57BL/6J
Mouse Uterus (E5.5)
Cell Sorting
Library Preparation and Sequencing
B
Dam Body Weight
Non−pregnant
Pregnant
Chow
HFHS
grams (g)
Weeks of diet
GD
C
Preconception Adiposity
Week 0
Week 10
% of body weight
Chow
HFHS
Diet
D
SDZ
PDZ
Em
500μm
E
Integrated
Chow
HFHS
UMAP 2
UMAP 1
72,349 cells
33,556 cells
38,793 cells
S1
S2
S3
S4
S5
uNK
T
ILC−Like
Mφ
cDC1
cDC2
Endo1
Endo2
Epi
Meso
SMC

485 **Figure 2: Identification of HFHS-induced transcriptional differences in E5.5 uterine cells**

486 (**A**) Pearson correlation coefficients (PCC) heatmap of Chow and HFHS diet groups. (**B**) Bar plots showing the
487 number of differentially expressed genes (DEGs) for each uterine cell type as a function of diet. Cess types: Hand2^{+}
488 endometrial stromal cells (ESCs); Hand2^{-} endometrial stromal cells (ESCs); uterine natural killer cells (uNK);
489 macrophage (Mφ); conventional dendritic cell 1 & 2 (cDC1, cDC2); innate lymphoid cell-like (ILC-like); T cells (T);
490 endothelial cell 1 & 2 (Endo1, Endo2); epithelial cell (Epi); mesothelial cell (Meso); smooth muscle cell (SMC). (**C**)
491 Scatter plots showing DEGs thresholded on adjusted p-val< 0.05 & and absolute Log2FC>0.5 in Hand2^{+} ESCs,
492 Hand2^{-} ESCs, uNK, and Mφ and the detection percentage of each cell type in Chow and HFHS groups. Number of
493 DEGs for each diet group are indicated. (**D**) Single-Cell Pathway Analysis using Hallmark gene sets obtained from
494 the Molecular Signatures Database for Hand2^{+} ESCs, Hand2^{-} ESCs, uNK, and Mφ. Blue dots signify more activity in
495 Chow, red dots signify enriched activity in HFHS, green dots signify activity in both Chow and HFHS. Qval: Q-value
496 indicating significance; Enrichment indicating extent of pathway enrichment relative to HFHS. Select pathways are
497 highlighted. EMT (Epithelial-to-mesenchymal transition); Ox. Phosp. (Oxidative phosphorylation); ROS (Reactive
498 oxygen species); KRAS Sig. (KRAS signaling). (**E**) Venn diagram showing DEGs specific to and shared with Hand2^{+}
499 ESCs, Hand2^{-} ESCs, uNK, and Mφ. Examples of genes unique to each cell state are indicated.

500

Figure 2

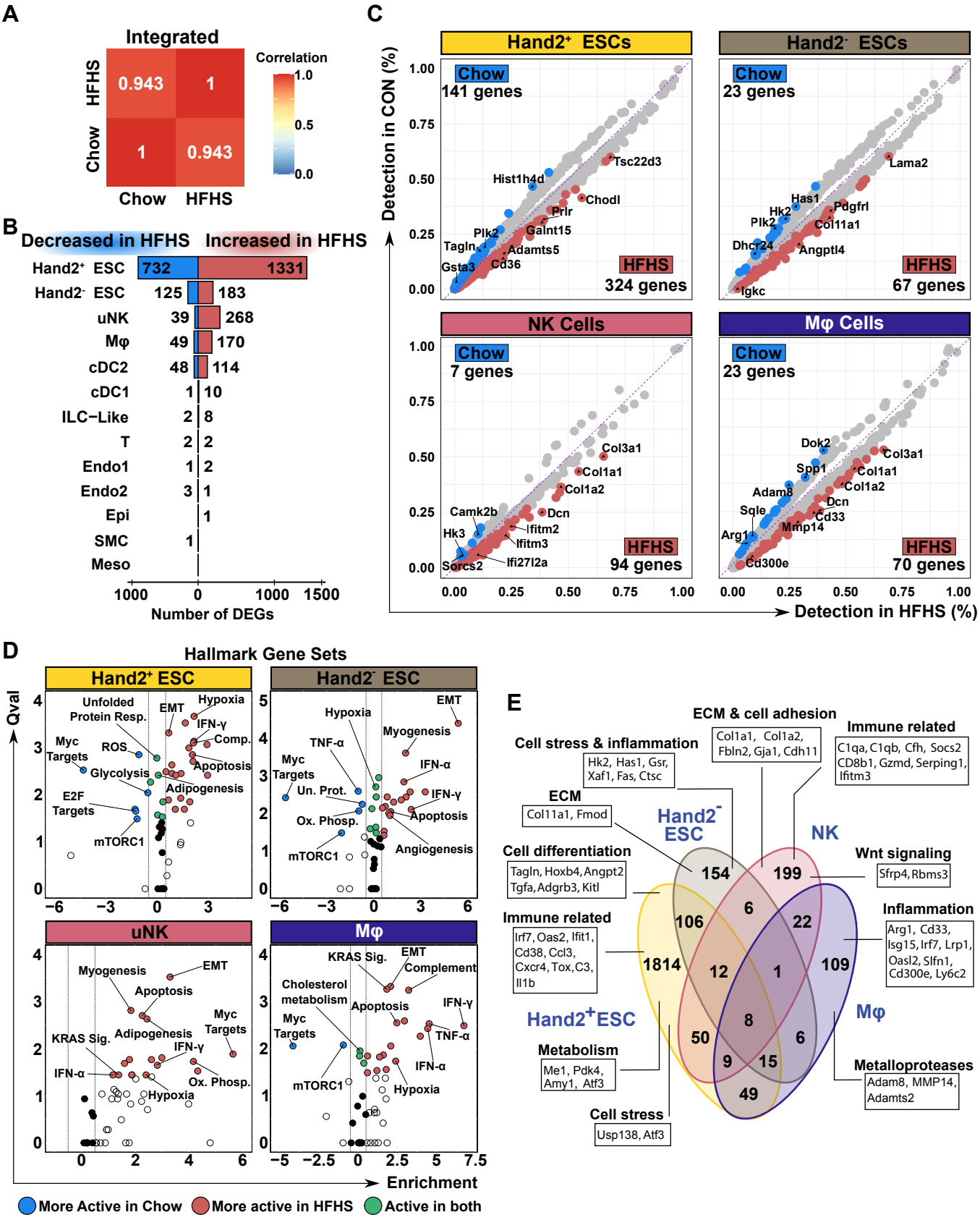
A
Integrated
HFHS
Chow
0.943
1
1
0.943
Chow
HFHS
Correlation
1.0
0.5
0.0
B
Decreased in HFHS
Increased in HFHS
Hand2+ ESC 732 1331
Hand2- ESC 125 183
uNK 39 268
Mφ 49 170
cDC2 48 114
cDC1 1 10
ILC−Like 2 8
T 2 2
Endo1 1 2
Endo2 3 1
Epi 1
SMC 1
Meso
1000 0 1000 1500
Number of DEGs
C
Hand2+ ESCs
Chow
141 genes
HFHS
324 genes
Tsc22d3
Hist1h4d
Chodl
Prlr
Galnt15
Plk2
Tagln
Adamts5
Gsta3
Cd36
Hand2- ESCs
Chow
23 genes
HFHS
67 genes
Lama2
Has1
Hk2
Pdgfrl
Plk2
Col11a1
Dhcr24
Angptl4
Igkc
NK Cells
Chow
7 genes
HFHS
94 genes
Col3a1
Col1a1
Col1a2
Dcn
Camk2b
Ifitm2
Hk3
Ifitm3
Sorcs2
Ifi27l2a
Mφ Cells
Chow
23 genes
HFHS
70 genes
Dok2
Col3a1
Spp1
Col1a1
Col1a2
Adam8
Dcn
Sqle
Cd33
Mmp14
Arg1
Cd300e
Detection in CON (%)
Detection in HFHS (%)
0.00 0.25 0.50 0.75 1.00
D
Hallmark Gene Sets
Hand2+ ESC
Unfolded Protein Resp.
EMT
Hypoxia
IFN-γ
Comp.
Myc Targets
ROS
Apoptosis
Glycolysis
Adipogenesis
E2F Targets
mTORC1
Hand2- ESC
EMT
Hypoxia
Myogenesis
TNF-α
Myc Targets
IFN-α
Un. Prot.
IFN-γ
Ox. Phosp.
Apoptosis
mTORC1
Angiogenesis
uNK
Myogenesis
EMT
Apoptosis
Myc Targets
KRAS Sig.
Adipogenesis
IFN-γ
IFN-α
Ox. Phosp.
Hypoxia
Mφ
KRAS Sig.
EMT
Complement
Cholesterol metabolism
Apoptosis
IFN-γ
Myc Targets
TNF-α
IFN-α
mTORC1
Hypoxia
Qval
Enrichment
More Active in Chow
More active in HFHS
Active in both
E
ECM & cell adhesion
Col1a1, Col1a2, Fbln2, Gja1, Cdh11
Immune related
C1qa, C1qb, Cfh, Socs2 CD8b1, Gzmd, Serping1, Ifitm3
Cell stress & inflammation
Hk2, Has1, Gsr, Xaf1, Fas, Ctsc
ECM
Col11a1, Fmod
Hand2- ESC
NK
Cell differentiation
Tagln, Hoxb4, Angpt2 Tgfa, Adgrb3, Kitl
Wnt signaling
Sfrp4, Rbms3
Immune related
Irf7, Oas2, Ifit1, Cd38, Ccl3, Cxcr4, Tox, C3, Il1b
Inflammation
Arg1, Cd33, Isg15, Irf7, Lrp1, Oasl2, Slfn1, Cd300e, Ly6c2
Hand2+ESC
Mφ
Metabolism
Me1, Pdk4, Amy1, Atf3
Metalloproteases
Adam8, MMP14, Adamts2
Cell stress
Usp138, Atf3
154
199
106
6
22
1814
12
1
109
8
50
6
9
15
49

501 **Figure 3: Maternal obesity leads to increased pro-inflammatory and immune-modulating pathways**
502 **in *Hand2*$^{+}$ ESCs**
503 (**A**) UMAP plot of 44,950 *Hand2*$^{+}$ endometrial stromal cells. UnStr: Undifferentiated Stromal Cells; PDZ1 & PDZ2:
504 Primary Decidual Zone clusters 1 & 2; SDZ1 and SDZ2: Secondary Decidual Zone clusters 1 & 2. (**B**) Bar plots
505 showing the numbers of DEGs in subtypes of *Hand2*$^{+}$ ESCs. (**C**) Venn diagram showing unique and shared DEGs
506 expressed in UnStr, PDZ2, and SDZ2 cell states. Highlighted are examples of DEGs specific to each cluster. (**D**)
507 Scatter plots showing DEGs in *Hand2*$^{+}$ ESC states thresholded on adjusted p-val< 0.05 and absolute Log2FC>0.5.
508 (**E**) Dot plot showing relative transcript levels of *Unc13c* and *Nos1* in *Hand2*$^{+}$ endometrial stromal cells. The
509 percentage of cluster-specific cells expressing each gene is indicated by dot size. H= HFHS diet; C= Chow diet. (**F**)
510 *In situ* hybridization images of *Unc13c* (blue signal), *Nos1* (blue signal), and *Hand2* (pink signal) in E5.5 implantation
511 sites. Bar = 100 μm. (**G**) Single-Cell Pathway Analysis of UnStr, PDZ2, and SDZ2 cell states from Chow and HFHS
512 mice. EMT: Epithelial-to-mesenchymal transition; Comp: Complement; Ox. Phosp.: Oxidative phosphorylation;
513 ROS: Reactive oxygen species; KRAS Sig.: KRAS signaling; Estrogen Resp.: Estrogen response. Blue dots signify more
514 activity in Chow, red dots signify enriched activity in HFHS, green dots signify activity in both Chow and HFHS. Qval:
515 Q-value indicating significance; Enrichment indicating extent of pathway enrichment relative to HFHS.
516

Figure 3

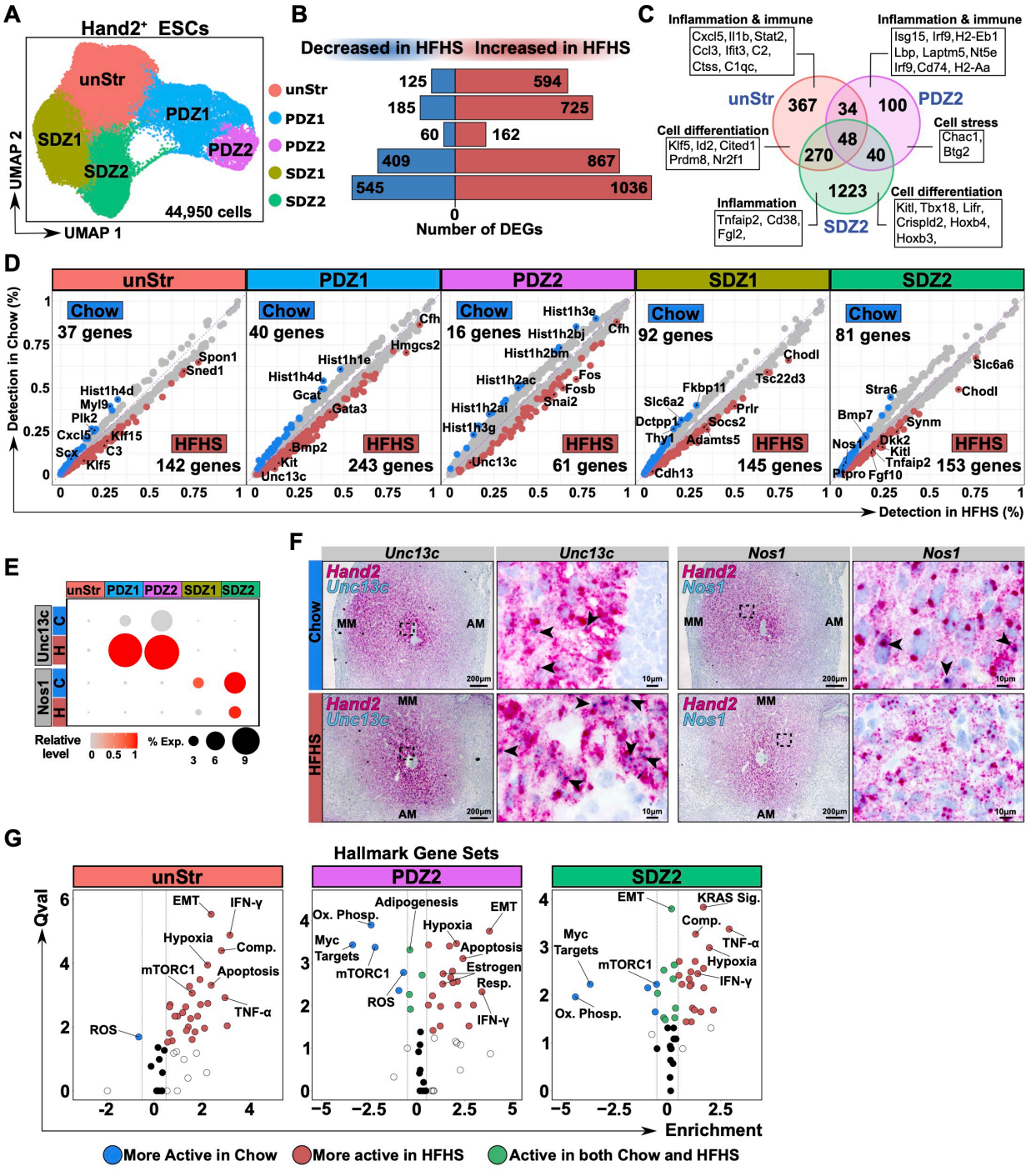
A
Hand2+ ESCs
unStr
PDZ1
PDZ2
SDZ1
SDZ2
44,950 cells
UMAP 2
UMAP 1
B
Decreased in HFHS
Increased in HFHS
125
594
185
725
60
162
409
867
545
1036
0
Number of DEGs
C
Inflammation & immune
Cxcl5, Il1b, Stat2, Ccl3, Ifit3, C2, Ctss, C1qc,
Inflammation & immune
Isg15, Irf9, H2-Eb1 Lbp, Laptm5, Nt5e Irf9, Cd74, H2-Aa
unStr
367
34
100
PDZ2
Cell differentiation
Klf5, Id2, Cited1 Prdm8, Nr2f1
48
Cell stress
Chac1, Btg2
270
40
1223
Inflammation
Tnfaip2, Cd38, Fgl2,
SDZ2
Cell differentiation
Kitl, Tbx18, Lifr, Crispld2, Hoxb4, Hoxb3,
D
unStr
PDZ1
PDZ2
SDZ1
SDZ2
Chow
37 genes
HFHS
142 genes
Spon1
Sned1
Hist1h4d
Myl9
Plk2
Cxcl5
Klf15
C3
Scx
Klf5
Chow
40 genes
HFHS
243 genes
Cfh
Hmgcs2
Hist1h1e
Hist1h4d
Gcat
Gata3
Bmp2
Kit
Unc13c
Chow
16 genes
HFHS
61 genes
Hist1h3e
Hist1h2bj
Cfh
Hist1h2bm
Hist1h2ac
Fos
Fosb
Snai2
Hist1h2ai
Hist1h3g
Unc13c
Chow
92 genes
HFHS
145 genes
Chodl
Tsc22d3
Fkbp11
Slc6a2
Prlr
Dctpp1
Socs2
Thy1
Adamts5
Cdh13
Chow
81 genes
HFHS
153 genes
Slc6a6
Stra6
Chodl
Bmp7
Synm
Nos1
Dkk2
Kitl
Tnfaip2
Ptpro
Fgf10
Detection in Chow (%)
Detection in HFHS (%)
E
unStr
PDZ1
PDZ2
SDZ1
SDZ2
Unc13c
C
H
Nos1
C
H
Relative level
0
0.5
1
% Exp.
3
6
9
F
Unc13c
Unc13c
Nos1
Nos1
Chow
HFHS
Hand2
Unc13c
Hand2
Nos1
MM
AM
200µm
10µm
G
Hallmark Gene Sets
unStr
PDZ2
SDZ2
Qval
EMT
IFN-γ
Hypoxia
Comp.
mTORC1
Apoptosis
TNF-α
ROS
Adipogenesis
Ox. Phosp.
Myc Targets
Estrogen Resp.
KRAS Sig.
Enrichment
More Active in Chow
More active in HFHS
Active in both Chow and HFHS

517 **Figure 4: Pseudotime modeling shows altered PDZ and SDZ differentiation kinetics in *Hand2*$^+$ cells**
518 (**A**) Monocle2-informed pseudotime ordering of *Hand2*$^+$ ESCs from Chow and HFHS mice. UnStr: Undifferentiated
519 Stromal Cells; PDZ1 and PDZ2: Primary Decidual Zone clusters 1 & 2; SDZ1 and SDZ2: Secondary Decidual Zone
520 clusters 1 & 2; snSF: Senescent Stromal Fibroblasts. (**B**) Monocle2-informed pseudotime ordering of subsetted
521 *Hand2*$^+$ cells from Chow and HFHS mice. (**C**) Heatmaps showing diet-associated patterns of 38 DEGs across
522 Monocle2-inferred pseudotime of *Hand2*$^+$ cells from Chow and HFHS mice. A pseudotime value of "0" depicts the
523 origin and arrows indicate direction of cell differentiation from the origin to either the PDZ or SDZ states. Genes
524 used to define pseudotime-predicted differentiation states (UnStr = *Fmod, Vim, Sfrp4;* PDZ = *Dio3, Id1, Ran*; SDZ =
525 *Mef2a, Rb1cc1,* Map2) are indicated with gray background. (**D**) Swarm and density plots showing cell densities
526 along PDZ and SDZ trajectories constructed using Slingshot. Kolmogorov-Smirnov test was performed to compare
527 distribution between two conditions along the pseudotime. p = *p* value; D = D-statistic. (**E**) *In situ* hybridization
528 images of *Hand2* transcript in E5.5 implantation sites of Chow and HFHS mice. Bar = 200 μm. MM = mesometrial
529 pole; AM = anti-mesometrial pole. (**F**) Bar plots showing quantification of *Hand2* signal area (μm^2) E5.5 implanation
530 sites, number of Hand2 probes per cell in the SDZ region, and cell size/area (μm^2) and number of cells within the
531 PDZ region. Means +/- standard deviations. Exact p-values are shown.
532

Figure 4

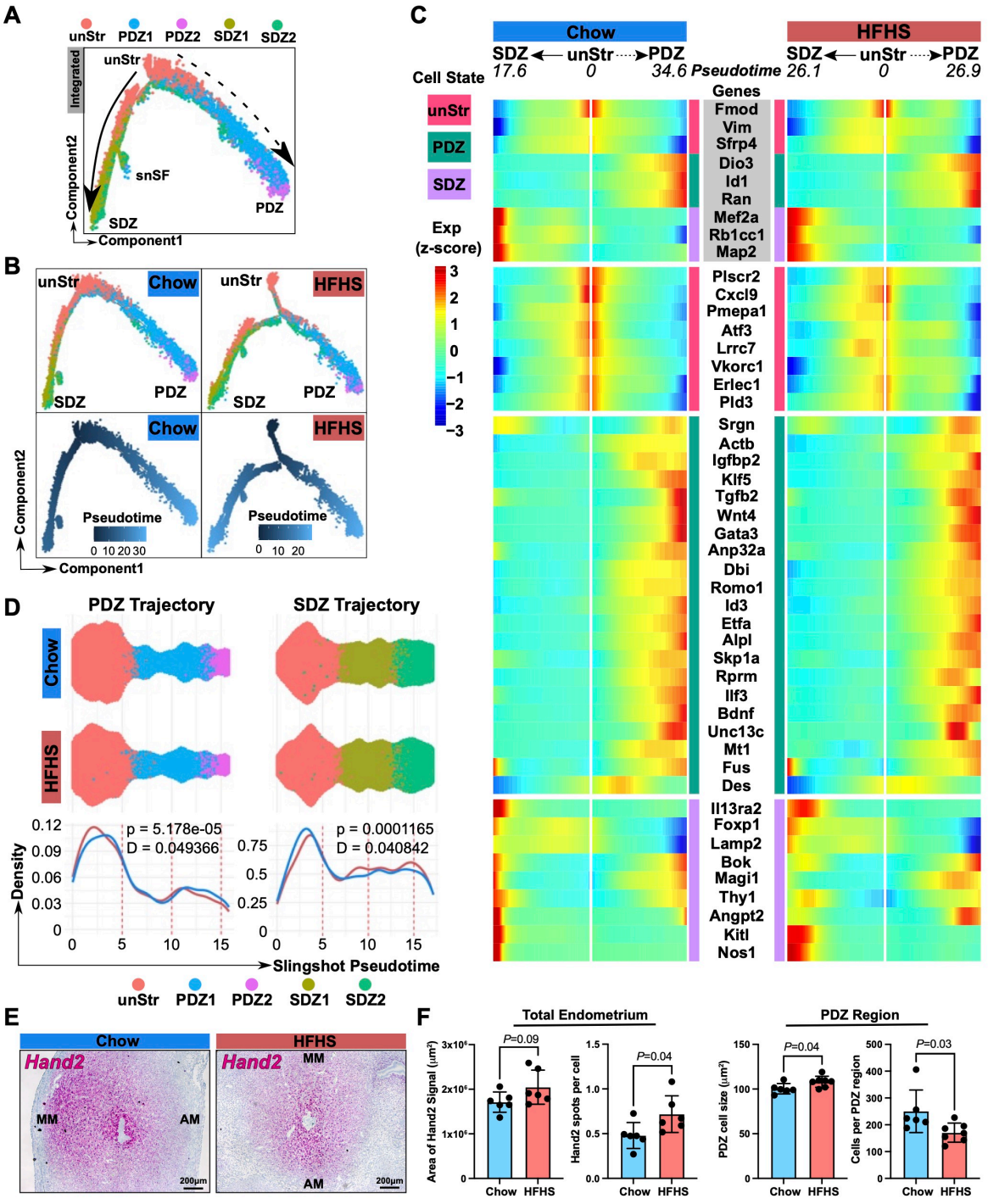
A
unStr PDZ1 PDZ2 SDZ1 SDZ2
Integrated
unStr
snSF
SDZ
PDZ
Component2
Component1
B
unStr
Chow
HFHS
SDZ
PDZ
Pseudotime
0 10 20 30
0 10 20
Component2
Component1
C
Chow
HFHS
SDZ ← unStr ···→ PDZ
17.6 0 34.6 Pseudotime
26.1 0 26.9
Cell State
unStr
PDZ
SDZ
Genes
Exp (z-score)
3 2 1 0 −1 −2 −3
Fmod
Vim
Sfrp4
Dio3
Id1
Ran
Mef2a
Rb1cc1
Map2
Plscr2
Cxcl9
Pmepa1
Atf3
Lrrc7
Vkorc1
Erlec1
Pld3
Srgn
Actb
Igfbp2
Klf5
Tgfb2
Wnt4
Gata3
Anp32a
Dbi
Romo1
Id3
Etfa
Alpl
Skp1a
Rprm
Ilf3
Bdnf
Unc13c
Mt1
Fus
Des
Il13ra2
Foxp1
Lamp2
Bok
Magi1
Thy1
Angpt2
Kitl
Nos1
D
PDZ Trajectory
SDZ Trajectory
Chow
HFHS
p = 5.178e-05
D = 0.049366
p = 0.0001165
D = 0.040842
Density
0.12 0.09 0.06 0.03 0
0.75 0.5 0.25 0
0 5 10 15
Slingshot Pseudotime
unStr PDZ1 PDZ2 SDZ1 SDZ2
E
Chow
HFHS
Hand2
MM
AM
200μm
F
Total Endometrium
PDZ Region
P=0.09
P=0.04
P=0.04
P=0.03
Area of Hand2 Signal (μm²)
Hand2 spots per cell
PDZ cell size (μm²)
Cells per PDZ region
Chow HFHS

533 **Figure 5: Maternal obesity drives alterations in endometrial stromal cell – immune cell interactions**
534 (**A**) CellChat ligand-receptor analysis of mouse uterine scRNA-seq data. Number and strength of overall
535 interactions between *Hand2*$^+$ endometrial stromal cell subsets, uNK, and Mφ. Line colour indicates whether the
536 interaction is increased (red) or decreased (blue) in HFHS. Arrows indicate interaction direction and line thickness
537 correlates the magnitude of interaction number or strength. (**B**) Top ligand-receptor associated signaling pathways
538 enriched in Chow and HFHS cells. P-value and relative contribution (Rel. Cont.) for each pathway are shown. (**C**)
539 Circle plots representing the top 50% aggregated interactions for the desmosterol signaling pathway between
540 *Hand2*$^+$ cells, uNK, Mφ in Chow and HFHS mice. Line colour indicates the cell type identify of the sender (blue =
541 PDZ1; pink = PDZ2), arrow indicates directionality of the cell-cell interaction, and line thickness correlates with
542 interaction strength. (**D**) Violin plots showing expression level of ligand/receptor (L-R) DEGs of the desmosterol
543 pathway in *Hand2*$^+$ stromal cells, uNK and Mφ. Box plots show 25th and 75th percentiles, and the black line indicates
544 median transcript levels. (**E**) Circle plots representing the top 50% aggregated interactions for the galectin signaling
545 pathway between *Hand2*$^+$ cells, uNK and Mφ in Chow and HFHS mice. Line colour indicates the cell type identify
546 of the sender (red = UnStr; blue = PDZ1; pink = PDZ2; dark green = SDZ1; light green = SDZ2; dark red = uNK; purple
547 = Mφ), arrow indicates directionality of the interaction, and line thickness correlates with interaction strength. (**F**)
548 Violin plots showing transcript levels of ligand/receptor (L-R) DEGs between Chow and HFHS mice of the galectin
549 signalling pathway. Box plots show 25th and 75th percentiles, and the black line indicates median expression level.
550
551

Figure 5

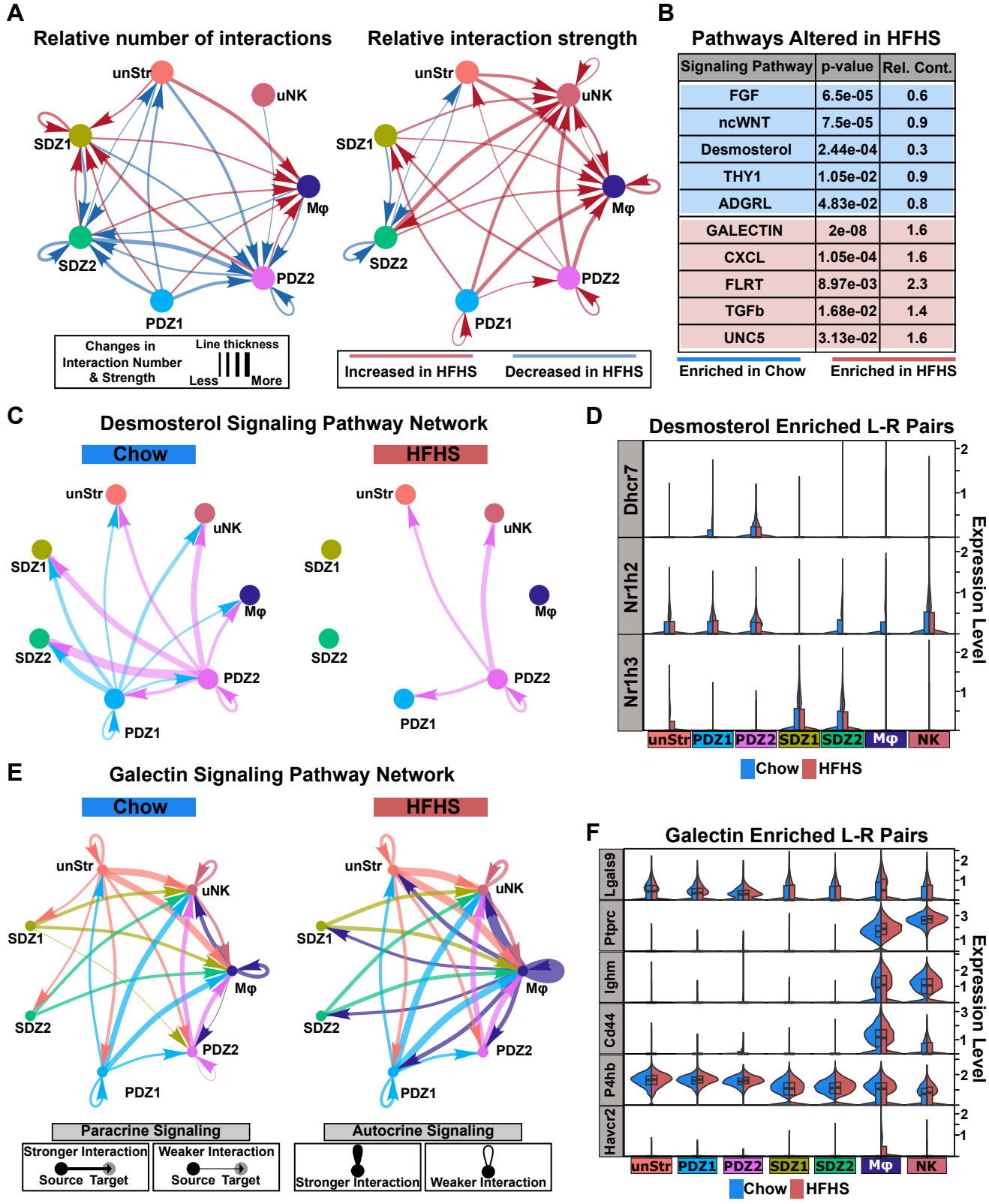
A
Relative number of interactions
Relative interaction strength
unStr
uNK
SDZ1
Mφ
SDZ2
PDZ2
PDZ1
Changes in Interaction Number & Strength
Line thickness
Less
More
Increased in HFHS
Decreased in HFHS
B
Pathways Altered in HFHS
Signaling Pathway | p-value | Rel. Cont.
FGF | 6.5e-05 | 0.6
ncWNT | 7.5e-05 | 0.9
Desmosterol | 2.44e-04 | 0.3
THY1 | 1.05e-02 | 0.9
ADGRL | 4.83e-02 | 0.8
GALECTIN | 2e-08 | 1.6
CXCL | 1.05e-04 | 1.6
FLRT | 8.97e-03 | 2.3
TGFb | 1.68e-02 | 1.4
UNC5 | 3.13e-02 | 1.6
Enriched in Chow
Enriched in HFHS
C
Desmosterol Signaling Pathway Network
Chow
HFHS
D
Desmosterol Enriched L-R Pairs
Dhcr7
Nr1h2
Nr1h3
Expression Level
unStr
PDZ1
PDZ2
SDZ1
SDZ2
Mφ
NK
Chow
HFHS
E
Galectin Signaling Pathway Network
Chow
HFHS
Paracrine Signaling
Stronger Interaction
Weaker Interaction
Source
Target
Autocrine Signaling
Stronger Interaction
Weaker Interaction
F
Galectin Enriched L-R Pairs
Lgals9
Ptprc
Ighm
Cd44
P4hb
Havcr2
Expression Level
unStr
PDZ1
PDZ2
SDZ1
SDZ2
Mφ
NK
Chow
HFHS

552 **SUPPLEMENTAL FIGURE TITLES AND LEGENDS**

553 **Figure S1: Obesogenic mouse model assessment and single-cell data quality control**

554 (**A**) Body weight measurements in grams (g) of dams subjected to 0 and 12 weeks of diet pre-pregnancy and at
555 plug detection (E0.5). Statistical analyses between groups were performed using two-way ANOVA followed by
556 Tukey's multiple comparisons test. *= $p < 0.01$. (**B**) Peri-ovarian adiposity as percent of total body weight following
557 12 weeks Chow or HFHS diet at E5.5. Analyses between groups were performed using Welch's t-test. * = $p<0.0001$.
558 (**C**) Violin plots showing the distribution of the number of genes (nFeature_RNA), Unique Molecular Identifiers
559 (#UMIs, nCount_RNA), and mitochondrial DNA percentage (%MtRNA) after quality control and data pre-
560 processing for each sample. Box plots indicate 25th and 75th percentiles, and the black line indicates data median.
561 Individual samples are denoted on the x axis (C = Chow or OB = obesogenic diet). (**D**) Dot plot showing the average
562 log expression level (colour) and proportion of cells expressing (dot size) of select genes used for determining the
563 cell type. (**E**) Pie charts showing the proportion of each cell cluster in Chow and HFHS groups. (**F**) Stacked bar plots
564 plotting the frequencies of *Hand2*$^{+}$, *Hand2*$^{-}$, uNK, and Mϕ cell types in Chow and HFHS mice. Data analyzed using
565 Welch's t-test.

566

567 **Figure S2: HFHS-induced changes in gene pathways of *Hand2*$^{+/-}$ stromal and uNK and Mφ cell types**

568 (**A**) Linear regression showing the linear relationship between number of captured/sequenced single cells and the
569 number of differentially expressed genes (DEGs) in cell type/clusters determined in single-cell transcriptomic
570 analysis. Shown is the coefficient of determination (R^2) and P-value. (**B**) Heatmap showing absolute fold-change
571 differences of Hallmark gene sets showing enrichment in *Hand2*$^{+}$, *Hand2*$^{-}$, uNK, and Mϕ cell types in relation to
572 Chow or HFHS diet. Blue = more active in Chow; Red = more active in HFHS. ** denotes pathways significantly
573 different (adjusted p-value < 0.01; absolute FC > 0.5) between Chow and HFHS diet conditions for each cell type.

574

575 **Figure S3: Cell subset identification, pathway analyses, and gene verification in Hand2^{+} stromal cells**

576 (**A**) Dot plot showing average log-transformed transcript levels (Av. Exp) of select genes used in identifying cell
577 identities of *Hand2*$^{+}$ undifferentiated endometrial stromal cells (ESC), primary decidual zone stromal cells, and
578 secondary decidual zone stromal cells. The proportion of cells (% Exp) within each cell state expressing each gene
579 is denoted by dot size. (**B**) Pie chart depicting the proportions of undifferentiated endometrial stromal cells
580 (UnStr), primary decidual zone cells (PDZ), and secondary decidual zone cells (SDZ) in Chow and HFHS mice. (**C**)
581 UMAP plots showing log-transformed mRNA levels of *Unc13c* and *Nos1* in Chow and HFHS in *Hand2*$^{+}$ endometrial
582 stromal cell subsets in UMAP space. (**D**) *In situ* hybridization images of positive (*Ppib*, blue signal; *Polr2a,* red signal)
583 and negative (scrambled oligo) control probes in E5.5 implantation sites. Bar = 100 μm. (**E**) Single-Cell Pathway
584 Analysis showing enriched Hallmark gene sets in PDZ1 and SDZ1 *Hand2*$^{+}$ cell states (Adjusted p-value < 0.01,

585 absolute FC > 0.5). Blue dots = more active in Chow; Red dots = more active in HFHS; Green dots = active in both
586 Chow and HFHS. Qval: Q-value indicating significance level. Select pathways are highlighted by lines. EMT:
587 Epithelial-to-mesenchymal transition; Comp: Complement; Ox. Phosp.: Oxidative phosphorylation; ROS: Reactive
588 oxygen species pathway.
589
590 **Figure S4: Monocle2, Monocle3, and Slingshot pseudotime ordering of *Hand2*⁺ stromal cells**
591 (**A**) Monocle2 pseudotime ordering of Chow and HFHS (integrated) *Hand2*⁺ stromal cells. Shade of cell along the
592 trajectory denotes pseudotime value. UnStr: Undifferentiated Stromal Cells; PDZ1 & PDZ2: Primary Decidual Zone
593 clusters 1 & 2; SDZ1 & SDZ2: Secondary Decidual Zone clusters 1 & 2, snSF: Senescent Stromal Fibroblasts. (**B**)
594 UMAP of *Hand2*⁺ stromal cells overlain with Monocle3-determined cell trajectories (black lines). (**C**) Monocle3-
595 determined pseudotime heatmap color gradient showing pseudotime values within UMAP space. (**D**) 3-
596 Dimensional rendering of *Hand2*⁺ stromal cell UMAP overlain with Monocle3-informed lineage trajectories (black
597 lines) showing PDZ and SDZ branches together or separately. (**E**) UMAP of *Hand2*⁺ stromal cells overlain with
598 Slingshot-determined lineage trajectories (black lines). Cells are colour coordinated by estimated Slingshot
599 pseudotime (red = early; blue = late) for integrated object.
600
601 **Figure S5: Identification of diet-driven alterations in cell-cell ligand-receptor interactions**
602 (**A**) Heatmap shows the net change in number of predicted ligand-receptor interactions (CellChat) between sender
603 (y-axis) and receiver (x-axis) cell populations, comparing HFHS to control conditions. Red and blue represent gains
604 and losses of interactions under HFHS, respectively. Bar graphs at the margins indicate the total number of
605 increased or decreased interactions per cell group, with values representing the total number of differentially
606 gained or lost ligand-receptor interactions. Significant ligand (L)-receptor (R) pairs between (**B**) SDZ2 (S2) and uNK
607 (NK) and (**C**) UnStr (U), PDZ1 (P1), PDZ2 (P2), and Mφ (M) cell types contributing to increased signaling in HFHS
608 diet. Dot color indicates communication probabilities (blue = low; red = high) and dot size indicates the p-value
609 (one-sided permutation test) of the activity of the L-R driven pathway in Chow or HFHS conditions. Arrows indicate
610 directionality of the ligand - receptor interaction between cell types.
611

Supplemental Figure 1

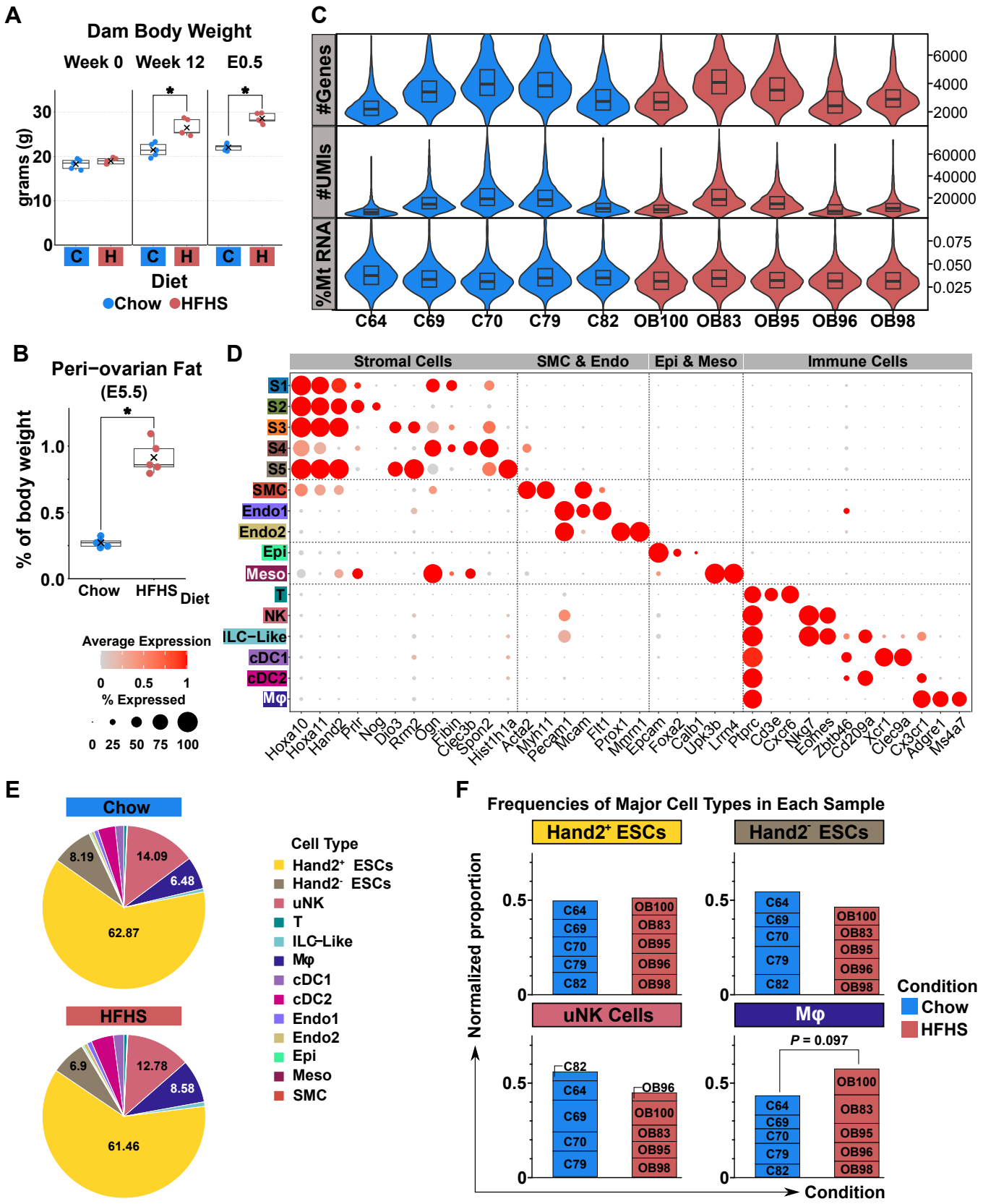

Supplemental Figure 2

A

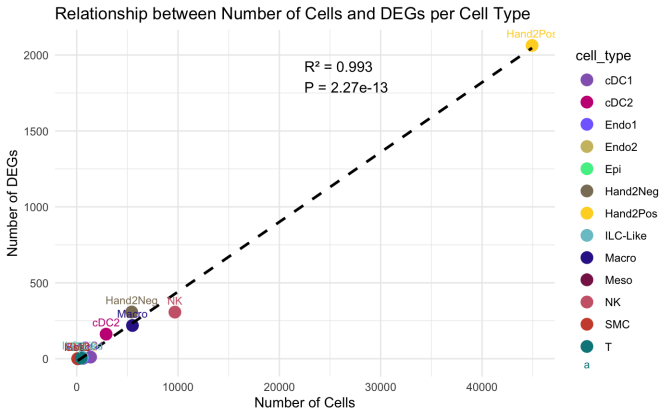

B

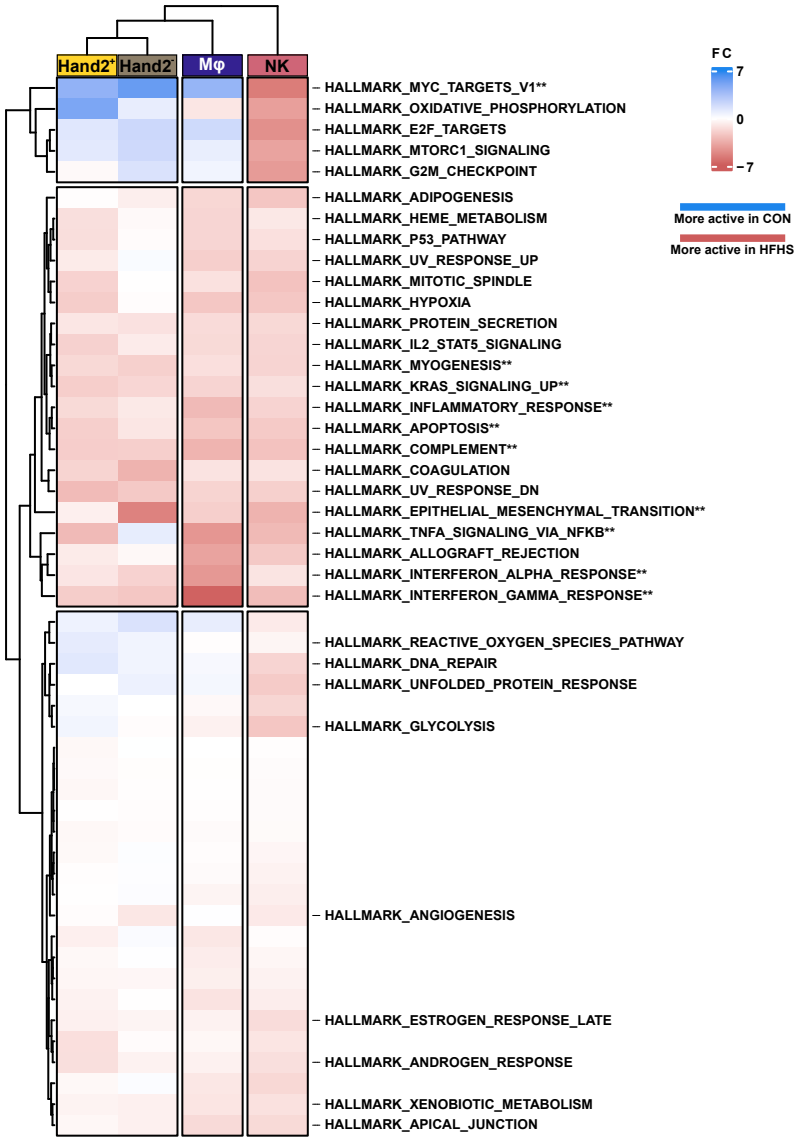

Supplemental Figure 3

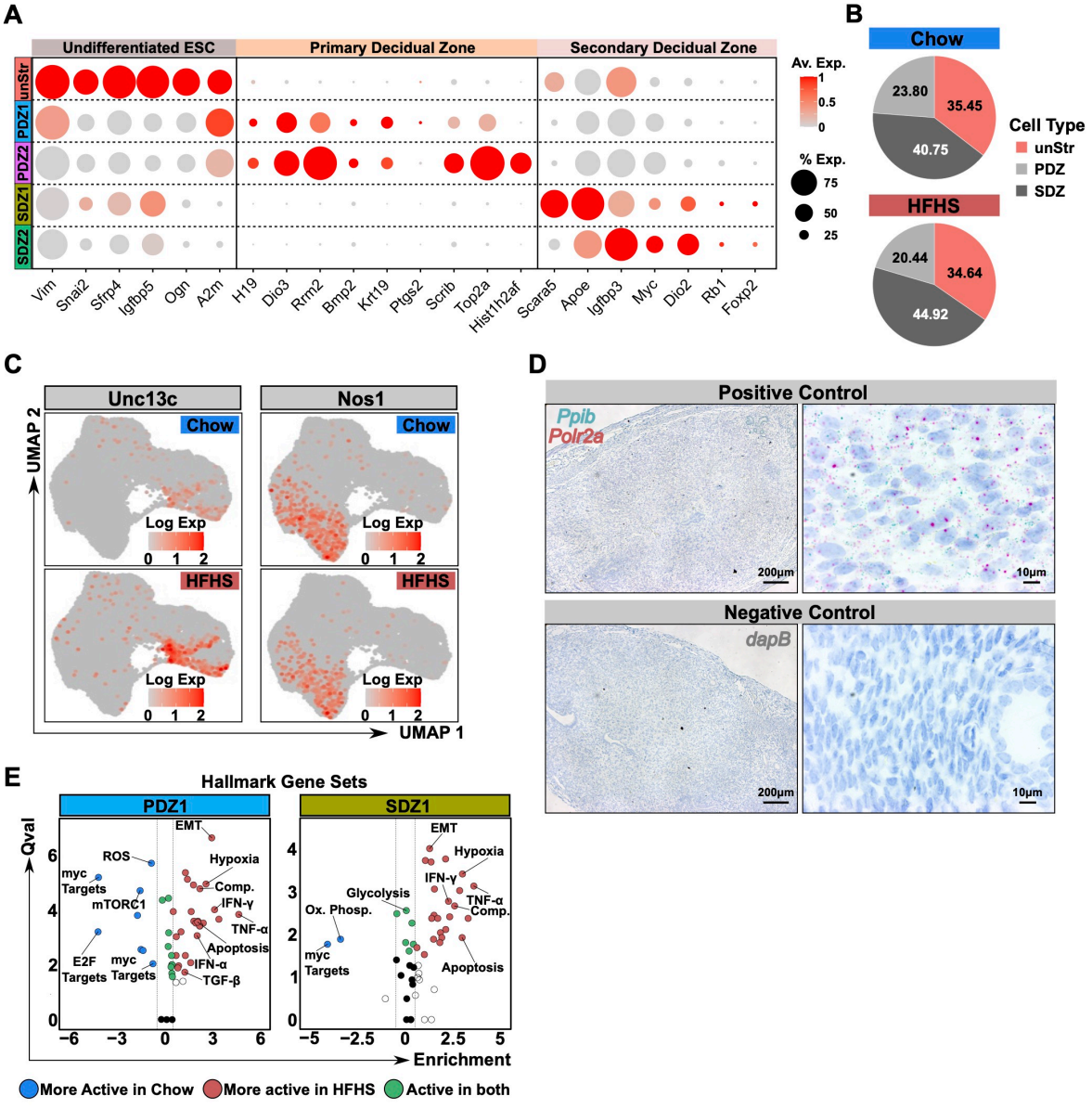

Supplemental Figure 4

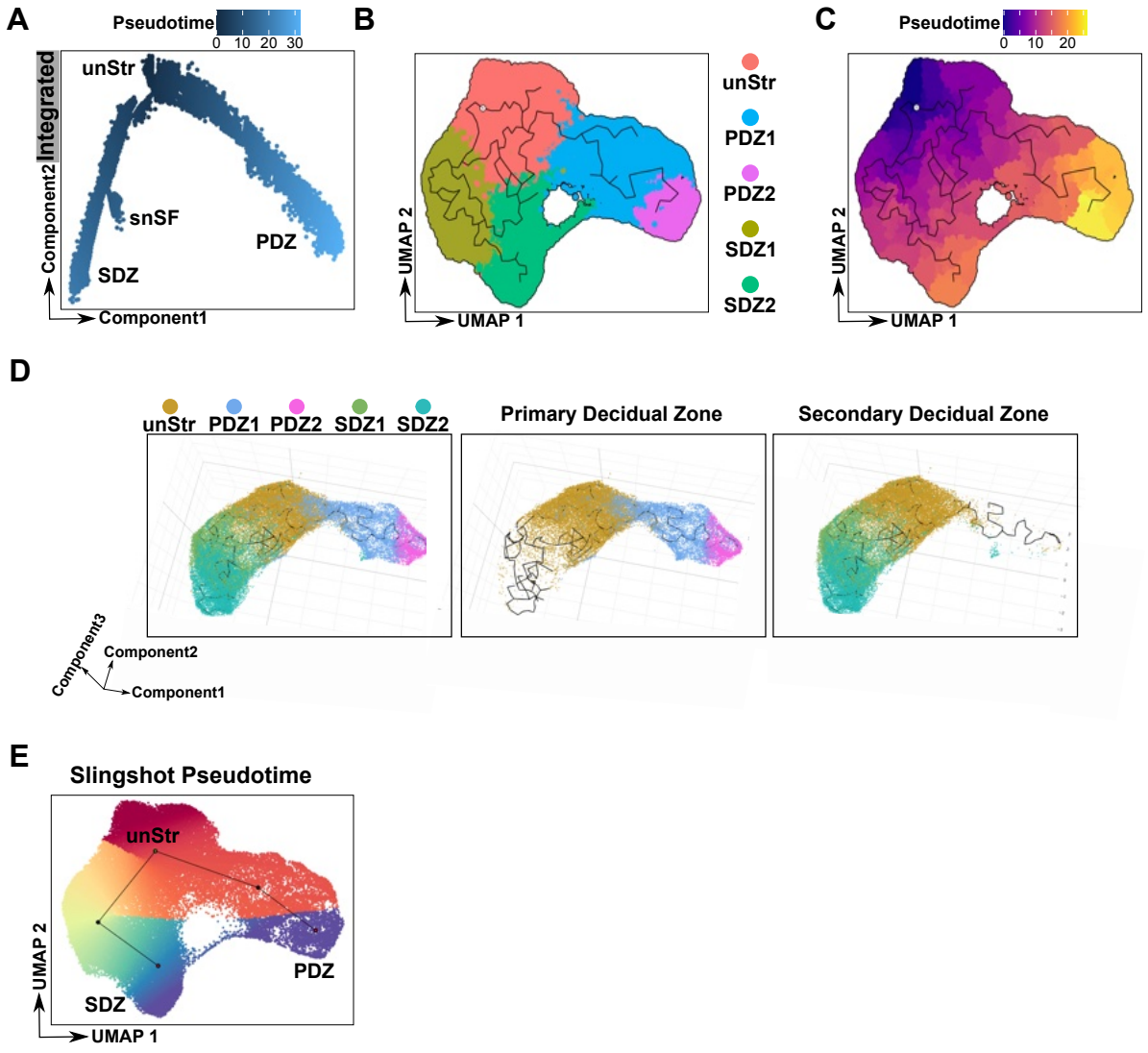

Supplemental Figure 5

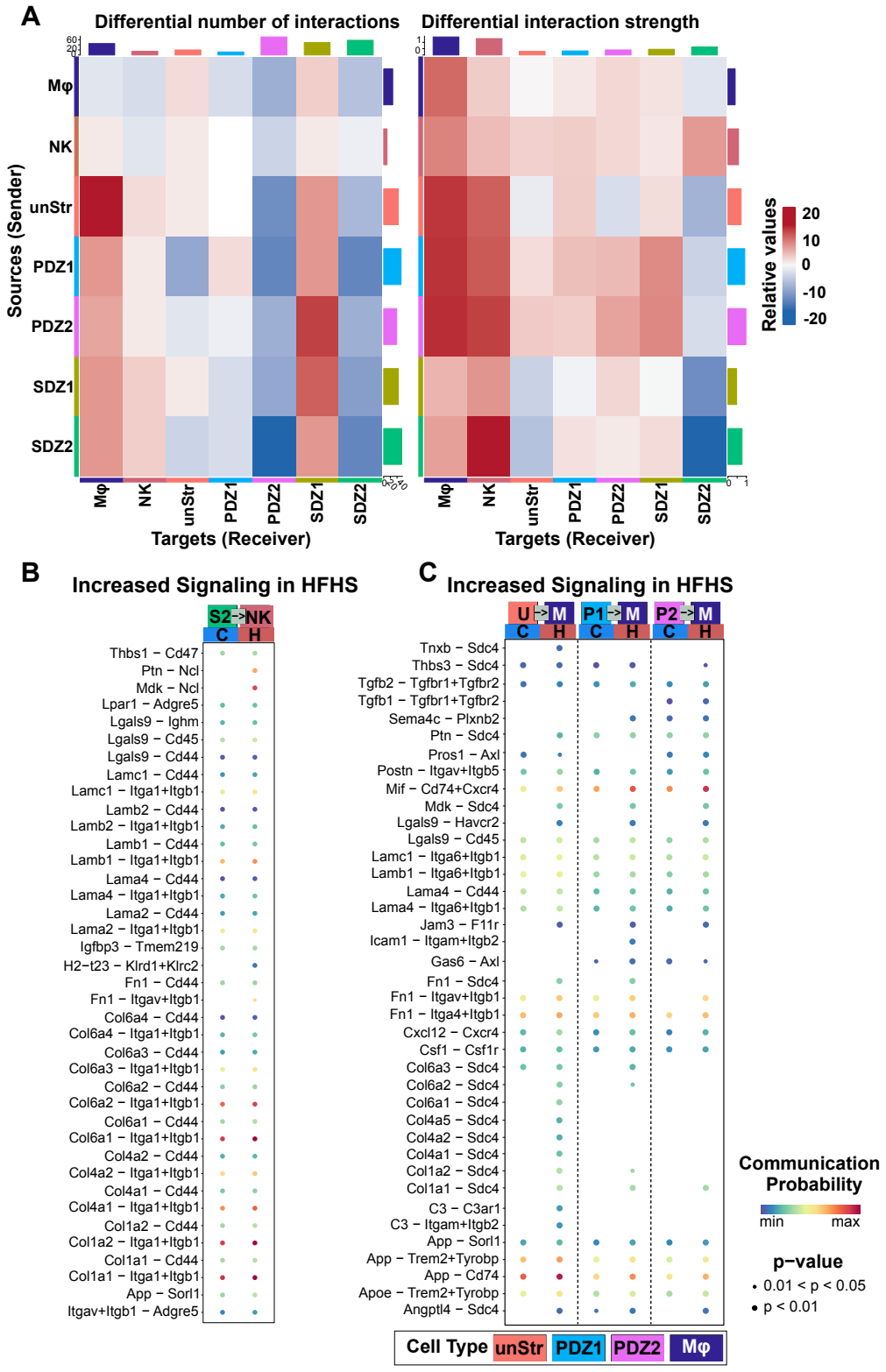

612 **METHODS**

613 **Key Resources Table**

REAGENT or RESOURCE	SOURCE	IDENTIFIER
Experimental models: Organisms/strains		
Mouse: C57BL/6J	The Jackson Laboratory	JAX:000664
Biological samples		
Mouse blood & E5.5 implantation sites	This paper	
Chemicals, peptides, and recombinant proteins		
Critical commercial assays		
Chromium Next GEM Chip G Single Cell Kit	10x Genomics	Cat#PN-1000120
Chromium Next GEM Single Cell 3' GEM, Library & Gel Bead Kit v3.1	10x Genomics	Cat#PN-1000123
Library Construction Kit	10x Genomics	Cat#PN-1000190
Chromium Next GEM Single Cell 3' Gel Bead Kit v3.1	10x Genomics	Cat#PN-1000122
Chromogenic RNAscope 2.5 HD Duplex Assay	ACD Bio	Cat#322430
Dual Index Kit TT Set A	10x Genomics	Cat#PN-1000215
SPRIselect Reagent Kit	Beckman Coulter	Cat#B23318
Agilent High Sensitivity DNA Kit	Agilent	Cat#5067-4626
Software and algorithms		
Seurat v5.0.0	Hao, Y. *et al.*	https://github.com/satijalab/seurat
Cell Ranger v6.0.1	10X Genomics	doi:10.1038/ncomms14049
scDblFinder v1.15.1	McGinnis, C. S. *et al.*	https://github.com/plger/scDblFinder
R v4.2.2	RDC Team	https://cran.r-project.org/
SCTransform v0.4.1	Hafemeister, C. *et al.*	https://github.com/satijalab/sctransform
Single-Cell Pathway Analysis v1.6.2	Bibby, J. A. *et al.*	https://jackbibby1.github.io/SCPA/
MAST v1.16.0	Finak, G. *et al.*	https://github.com/RGLab/MAST
Monocle2 v2.20.0	Trapnell, C. *et al.*; Qiu, X. *et al.*	https://github.com/cole-trapnell-lab/monocle-release
Monocle3 v2.26.0	Cao, J. *et al.*	https://github.com/cole-trapnell-lab/monocle3
Slingshot v2.6.0	Street, K. *et al.*	https://github.com/kstreet13/slingshot
ComplexHeatmap v2.14.0	Gu Z. *et al.*	https://github.com/jokergoo/ComplexHeatmap
CellChat v2.1.2	Jin, S. *et al.*	https://github.com/sqjin/CellChat
ShinyCell v2.1.0	Ouyang, J. F. *et al.*	https://github.com/SGDDNB/ShinyCell
Rsconnect v1.4.1	Atkins, A. *et al.*	https://rstudio.github.io/rsconnect/

ggplot2 v3.4.4	Wichkam, H. *et al*.	https://github.com/tidyverse/ggplot2/
Other		
Teklad 22/5 Rodent Diet	Envigo	Cat#8640
Rodent Diet With 45 kcal% Fat	Research Diets Inc.	D12451
Dynabeads ™ MyOne™ SILANE	Invitrogen	Cat#37002D
AxioObserver inverted microscope	Zeiss	N/A
BD FACSAria™ III Cell Sorter	BD Biosciences	N/A
Chromium Controller & Next GEM Accessory Kit	10X Genomics	N/A
Mm-Unc13c-C1	ACD Bio	Cat#501411
Mm-Nos1-C1	ACD Bio	Cat#418461
Mm-Hand2-C2	ACD Bio	Cat#418461
NextSeq 2000 instrument	Illumina	N/A
5X Plan-Apochromat objective/0.16NA objective	Zeiss	N/A
20X Plan-Apochromat/0.80NA objective	Zeiss	N/A
40X Plan-Apochromat/1.4NA objective	Zeiss	N/A
QuPath v0.6.0	Bankhead, P. et al.	https://qupath.github.io/
Interactive website for the publication	This paper	https://micematernalobesity.shinyapps.io/bk_maternalobesity_2025/

RESOURCE AVAILABILITY

Lead Contact

Alexander G Beristain takes responsibility for the lead contact role. All requests for additional information pertaining to the content of, or materials utilized in, this manuscript should be directed to, and will be addressed by, the lead contact Alexander G. Beristain aberista@mail.ubc.ca

Materials Availability

This study did not generate new unique reagents. C57BL/6J mice used in this study were purchased from the Jackson Laboratories (Bar Harbor, Maine, USA).

Data and Code Availability

- Single-cell RNA-seq data generated in this paper have been deposited at GEO and are publicly available as of the date of publication. The accession numbers for this newly synthesized dataset are listed in the key resources table. Processed sequencing data in the form of Seurat objects are available at: https://micematernalobesity.shinyapps.io/bk_maternalobesity_2025/
- This paper does not report original code. The computational pipelines used for all data processing and bioinformatic analyses in this paper has been deposited at Zenodo and is publicly available as of the date of publication. DOIs are listed in the key resources table.

633 • Any additional information required to reanalyze the data reported in this paper is available from the Lead
634 Contact upon request.
635
636 **Animal Model**
637 *Ethical statement*
638 All animal procedures for this study were approved by the McMaster University Animal Research Ethics
639 Board (Animal Utilization Protocol 20-07-27) and conducted in accordance with the guidelines of the Canadian
640 Council on Animal Care.
641 *Experimental animals*
642 Eight-week-old C57BL/6J female mice (Jackson Laboratories, strain 000664) were randomly assigned to
643 receive either a control rodent chow (Chow; 17% fat, 54% carbohydrate, 29% protein (kCal/g), n = 5; Envigo 8640)
644 or a high fat, high sucrose diet (HFHS; 45% fat, 17% sucrose, 18% carbohydrate, 20% protein (kCal/g), n = 5;
645 Research Diets D12451) *ad libitum* for a minimum of 12 weeks to induce preconception excess adiposity as
646 previously described[32,72,76]. Total fat mass and body weight were measured at baseline and following 10-weeks of
647 diet onset using a whole-body composition analyzer (Minispec LF90-II, Bruker) used to calculate total adiposity
648 relative to bodyweight. Following the dietary intervention, females were time-mated with Chow-fed C57BL/6J
649 males to generate pregnancies. The presence of a copulatory plug in the morning following timed mating was
650 designated embryonic day 0.5 (E0.5), and dams were singly housed until experimental endpoint at embryonic day
651 (E)5.5. At E5.5, dams were euthanized by cervical dislocation and tissues were collected for downstream analysis.
652
653 **Tissue collection and dissociation of uterine horns**
654 *Tissue Collection:* Immediately following euthanasia, laparotomy was performed, reproductive tissues were
655 collected, and uterine horns were dissected in Dulbecco's phosphate-buffered saline (D-PBS, pH 7.4; Wisent
656 Biosciences). The uterus was freed by making incisions at each utero-tubal junction and the cervix. One uterine
657 horn per dam was fixed in 4% w/v paraformaldehyde in D-PBS for 24 hours at room temperature, and the
658 remaining uterine horn was processed to generate single-cell suspensions.
659 *Histological confirmation of pregnancy:* Fixed uterine horns were processed for paraffin embedding and
660 sectioned at a thickness of 5 µm. The sections were stained with hematoxylin and eosin and examined under
661 brightfield illumination at 20× magnification using a Nikon NiE Eclipse Microscope. Samples displaying focal
662 distension of the uterine wall, lack of a continuous uterine lumen, and cytological changes consistent with
663 decidualization of endometrial stromal cells were used to confirm pregnancy.

664 *Tissue dissociation and generation of single cell suspensions:* One uterine horn per pregnancy was collected
665 to generate single cell suspensions for transcriptomic profiling using single-cell RNA sequencing (scRNAseq).
666 Tissues were rinsed in Penicillin and Streptomycin supplemented RPMI 1640 basal media (Wisent Biosciences) and
667 minced with scissors. Minced tissue was transferred to a volume of 2.5 ml of tissue digestion media (50 µg/mL
668 Liberase TM (0.28 Wünsch units) and 50 µg/ml DNase I in RPMI). Tissues were digested at 37°C for 30 minutes and
669 filtered through a 70-µm nylon cell sieve into 1mL of FBS. Suspensions were topped up to a volume of 20 mL with
670 RPMI (5% v/v FBS) and centrifuged at 350×g for 10 minutes. Cell pellets were washed and resuspended in 500 µl
671 of D-PBS, and live cell densities in each prep were determined by manual counting with a Neubauer
672 hemocytometer and Trypan Blue-stained aliquots (0.4%; Gibco). Suspensions were pelleted and resuspended in
673 FBS at a density of 2×10^6 live cells/ml. An equal volume of FBS containing 20% dimethyl sulfoxide (DMSO;
674 Millipore Sigma, D2650) was added to cell suspensions as cryoprotectant, for a final suspension of 1×10^6 cells/ml
675 in FBS + 10% DMSO. Samples were cryopreserved at -80°C, then transferred to long-term storage at -150°C until
676 library preparation.

677

678 **Generation of scRNAseq library**

679 *Sample preparation:* Cryopreserved cell suspensions from confirmed Chow and HFHS pregnancies (n = 5/group)
680 were rapidly thawed and freezing media removed by washing with RMPI media without glutamine and HEPES
681 (Gibco) supplemented with 10% FBS and 1% Pen/Strep. Cells were pelleted at 400g and resuspended in 500 µl of
682 cell sorting buffer (2% FBS in HBSS 1X Without calcium and magnesium) supplemented with 7-Aminoactinomycin
683 D (7-AAD, 1:40; eBioscience) for 20 minutes to stain dead cells and filtered using a 40 µm FlowMi cell strainer (Bel-
684 Art). Viable (7-AAD negative) cells were isolated using a BD FACS Aria cell sorter using a 100µm nozzle 20 PSI
685 thresholds. Cells were collected in 0.04% UltraPure BSA (Invitrogen) in PBS. Collected cells were used immediately
686 for preparation of single-cell RNA libraries using the Chromium Single Cell 3' v3.1 kit (10x Genomics) according to
687 the manufacturer's protocol (CG000315 Rev C) and sequenced on an Illumina NextSeq2000 platform targeting
688 ~60,000 reads per cell. Sequencing reads were aligned to *mus musculus* reference genome mm10-2.1.0 using
689 cellranger v6.0.1. A total of 97,414 cells were captured for sequencing (Chow n = 49,891 and HFHS n = 47,523) at
690 an average depth of ~60,000 sequencing reads/cell.

691

692 **scRNAseq data analysis**

693 *Data pre-processing & quality control:* Cells were pre-processed using the Seurat R package[37] (v5.0.0). To
694 exclude low-quality cells, cells with fewer than 1,000 or more than 7,500 detected genes, as well as cells with
695 greater than 10% mitochondrial transcript content were removed. Doublet detection was performed on individual

696 samples using the "scDblFinder" package[77] (v1.15.1), and predicted doublets were excluded from subsequent
697 analyses. Remaining cells were normalized and scored for cell cycle phase based on canonical G2/M and S phase
698 gene sets. To identify genes exhibiting high biological variability, the "FindVariableFeatures" function was applied
699 using the "vst" selection method, prioritizing the top 2,000 highly variable genes per sample. Data were scaled to
700 center expression values and regress out unwanted sources of variation before integration. Samples were
701 subsequently merged, split by dietary condition, and integrated using the "SCTransform"[78] v2 workflow. During
702 integration, the Pearson residuals obtained from the default regularized negative binomial model were re-
703 computed and scaled to remove latent variation resulting from the difference between the G2/M and S phase cell
704 cycle scores. After integration, data layers generated through SCTransform were combined into a single layer using
705 the "JoinLayers" function.
706
707 *Cell clustering and cell type annotation:*
708 • Integrated object: The top 50 principal components were used for dimensionality reduction and visualization
709 using the Uniform Manifold Approximation and Projection (UMAP) algorithm. Clustering of the single cells was
710 performed at a resolution of 0.24. Cell type annotation was completed by the expression of canonical marker
711 genes, in combination with differentially expressed genes identified using the "FindAllMarkers" function.
712 Marker genes were defined as those exhibiting a log2 fold-change (log2FC) greater 0.1 and an adjusted p-value
713 below 0.01 within a given cluster. If multiple clusters were determined to be same cell type, sub-index is added
714 to that cell type for each different original Seurat cluster. Endometrial stromal cells were determined by
715 expression of *Hoxa10* and *Hoxa11*, immune cells were identified by CD45 (*Ptprc*) expression. Cells expressing
716 *Pecam1* were annotated as endothelial cells, *Krt18* expressing cells were identified as epithelial cells, and *Acta2*
717 and *Myh11* expression was used to determine smooth muscle cells. UMAP plots were generated for integrated
718 object, Chow and HFHS subsets.
719 • Hand2^{+} ESC subset: Endometrial stromal cell clusters (ESCs) that were also expressing Hand2 were subset from
720 the integrated object and re-clustered in Seurat at a resolution of 0.23 using 30 principal components. Markers
721 were identified using the same strategy as the integrated object. Undifferentiated endometrial stromal cells
722 were annotated based on the expression of *Vim, Snai2, Sfrp4, Igfbp5*. Primary decidual zone (PDZ) clusters
723 were identified by the expression of *H19, Dio3, Krt19, Bmp2*, while secondary decidual zone (SDZ) clusters
724 were defined by the expression of *Scara5, Igfbp3, Dio2, Rb1, Foxp2*. Marker genes were defined by Seurat are
725 those exhibiting log2FC greater than 0.1 and an adjusted p-value below 0.01 within a given cluster.
726
727 *Pseudo-bulk Pearson's correlation coefficient analysis:* Expression matrices from the integrated dataset were
728 averaged by dietary condition and log-transformed to create ''pseudo-bulk'' gene expression profiles using

729 "AverageExpression" function. Pearson correlation coefficients between pseudo-bulk samples were calculated
730 using the "cor" function from the stats R package (v4.2.2).
731
732 *Differential gene expression:* Differential gene expression (DGE) analyses were performed using the
733 "FindMarkers" function in Seurat, implemented with the MAST statistical framework[79]. To maximize
734 transcriptome-wide detection sensitivity, parameter thresholds were set to include all genes regardless of their
735 expression frequency by specifying min.pct = -Inf and min.diff.pct = -Inf. Genes with adjusted p-value below 0.05
736 and exhibiting a log2FC greater than 0.2 between groups were reported in Figure 2B and Figure 3B. Differentially
737 expressed genes (DEGs) with log2FC greater than 0.5 were plotted as a scatterplot using ggplot2[80] (v3.4.4). The
738 default RNA assay was used for all analyses.
739
740 *Pathway analysis:* Pathway enrichment analysis was performed using a modified implementation of the Single-
741 Cell Pathway Analysis[81] (v1.6.2) package to evaluate the impact of maternal diet on cellular signaling pathways at
742 single-cell resolution. To increase statistical power and the number of cells contributing to pathway comparisons,
743 the "compare_seurat" function was adapted to allow a downsampling threshold of 3,000 cells per group (default
744 = 500). Gene signatures corresponding to Hallmark pathways were obtained from the msigdbr mouse datasets[82,83],
745 and formatted for SCPA using the "format_pathways" function. SCPA comparisons were performed across Hand2$^+$
746 ESCs, Hand2$^-$ ESCs, natural killer (NK) cells, and macrophages. Pathways enriched in either group with a fold change
747 (FC) > 0.5 and adjusted p-value < 0.01 were visualized using ggplot2[80] (v3.4.4). To compare pathway-level trends
748 across populations, FC values for each pathway were extracted from the SCPA outputs of Hand2$^+$ ESCs, Hand2$^-$
749 ESCs, NK, and macrophage, and a matrix containing combined matrix of enrichment scores was generated.
750 Significant pathways, defined as those meeting FC and adjusted p-value thresholds in at least one population,
751 were used to annotate heatmap rows. Heatmap was generated using the ComplexHeatmap R package[84] (v2.14.0),
752 displaying FC values across the four cell populations. Unsupervised k-means clustering was applied to both
753 pathways and populations to visualize shared or distinct pathway activity patterns. For Hand2$^+$ ESCs, pathway
754 enrichment was assessed using re-clustered object across dietary conditions considering each stromal cluster by
755 defining group1 as diet and group 2 as stromal cell subtypes, whereas for other populations enrichment was
756 compared across dietary condition across the entire cluster.
757 SCPA was also used to compare pathway activity in distinct Hand2$^+$ ESCs sub-types after re-clustering
758 (UnStr, PDZ1, PDZ2, SDZ1, and SDZ2). Pathways enriched in either group with a FC greater than 0.5 and adjusted
759 p-value less than 0.01 were plotted using ggplot2[80] (v3.4.4).
760
761 *Pseudotime Analysis:* The Monocle2 R package[85] (v2.26.0), Monocle3 R package[86] (v1.3.1), and Slingshot R

762 package[58] (v2.6.0) were used to explore the differentiation of undifferentiated ESCs to PDZ and SDZ endpoints in
763 Hand2$^+$ ESCs.

764 1) *Monocle2:* Re-clustered Hand2$^+$ ESC v5 RNA assay was first converted to a Monocle2-compatible v3 RNA assay
765 following the standard Seurat RNA5-to-RNA3 pipeline and Seurat object was subsequently converted to
766 CellDataSet object using "as.CellDataSet" function. Cells were then imported into monocle2 to perform semi-
767 supervised single-cell ordering in pseudotime using Sfrp4, Igfbp5, Sparc, Fst, Mfap4, Ogn, Fos to denote cells
768 at the origin. Progression towards PDZ was characterized by Dio3, Id3, and Ran whereas progression towards
769 SDZ was characterized by Scara5, Apoe, and Inmt. Branched expression analysis modelling (BEAM) was applied
770 to assess gene expression dynamics along bifurcating pseudotime trajectories progressing towards PDZ or SDZ
771 maturation. Trajectory graphs were constructed by first reducing dimensions using "reduceDimension"
772 function, followed by "orderCells" function to order cells in pseudotime designating UnStr as the origin based
773 on the known transcriptomic markers. Trajectory ordering and structures were visualized using
774 "plot_cell_trajectory" function. For comparative analyses, re-clustered Hand2$^+$ ESCs were further subset based
775 on dietary condition (Chow and HFHS) in order to generate diet-specific single-cell pseudotime ordering, and
776 independent trajectories were constructed using the same genes and gene expression thresholds for diet-
777 specific comparison. In order to test each gene for differential expression analysis as a function of pseudotime,
778 differential gene test was performed with the object containing both Chow and HFHS cells using
779 "differentialGeneTest" function by combining monocle2 pseudotime and diet information as covariates, and
780 select genes were plotted using "plot_genes_branched_heatmap" function for Chow and HFHS objects along
781 the pseudotime.

782 2) *Monocle3:* For trajectory modeling with Monocle3, re-clustered Hand2$^+$ ESC expression matrices were
783 imported, clustered, and used to create the principal graph with the "learn_graph" function. Cells were
784 ordered in pseudotime using "order_cells" function with the trajectory root designated based on the root cell
785 ID identified in the corresponding Monocle 2 analysis. To visualize lineage trajectories in three-dimensional
786 space, "plot_cells_3d" function was used and two distinct, branching trajectories corresponding to PDZ and
787 SDZ maturation was shown.

788 3) *Slingshot:* To perform trajectory modeling using Slingshot, re-clustered Hand2$^+$ ESC object was converted to a
789 SingleCellExperiment object using "as.SingleCellExperiment" function. Lineages were constructed in UMAP
790 space using the "slingshot" function, with the unStr cluster specified as the starting point and PDZ2 and SDZ2
791 clusters as the endpoints. A stretch factor of 0 and default lineage extension parameters were applied.
792 Pseudotime values along each lineage were calculated and visualized by projecting cells onto the UMAP
793 embedding, with colors representing pseudotime values for each cell. Lineage curves were overlaid using the
794 lines function from Slingshot to illustrate differentiation pathways, and pseudotime_1 and pseudotime_2

795 values were plotted in UMAP space. For comparative analyses, re-clustered Hand2$^+$ ESCs were further subset
796 based on their cluster identity. The UnStr, PDZ1 and PDZ2 were used to generate PDZ- specific single-cell
797 pseudotime ordering while UnStr, SDZ1, and SDZ2 were subset to model SDZ-specific pseudotime ordering.
798 Independent trajectories were constructed using the same parameters used for the initial integrated analysis.
799 To assess the effect of maternal diet on ESC differentiation, pseudotime distributions along the PDZ and SDZ
800 trajectories were compared between Maternal Chow and HFHS groups using a density plot generated with
801 ggplot2[80] (v3.4.4), and statistical significance was assessed using the Kolmogorov-Smirnov Test using "ks.test"
802 function from stats R package (v4.2.2).
803
804 *Cell-cell interaction analysis:* Cell-cell communication was analyzed using CellChat R package[59] (v2.1.2) to infer
805 ligand-receptor signaling networks in early post-implantation mice uterus following the author's pipeline. Object
806 containing between Hand2$^+$ ESC subsets, NK and macrophages was subset based on diet, and Chow and HFHS
807 independently processed using CellChat to create Chow and HFHS data objects containing inferred interactions.
808 Normalized gene expression matrix and cell-level metadata were provided as input to CellChat, with group
809 identities defined by stromal subset annotation. The default ligand-receptor interaction database for mouse
810 "CellChatDB.mouse" was used to infer potential intercellular communications. Overexpressed genes and ligand-
811 receptor interactions were identified using the "subsetData", "identifyOverExpressedGenes", and
812 "identifyOverExpressedInteractions" functions. Communication probabilities were computed using the trimean
813 method "computeCommunProb" and filtered for interactions using "filterCommunication" containing at least 10
814 cells per interacting group. Inferred communications were aggregated at both the ligand-receptor pair and
815 signaling pathway levels using "computeCommunProbPathway" and "aggregateNet". Network centrality analysis
816 was performed to assess signaling roles of each cell group, and significant communication networks were
817 visualized using circle plots "netVisual_aggregate".
818 Differential communication analyses between dietary conditions were conducted by merging CellChat
819 objects with "mergeCellChat", followed by comparative network visualization of top 50% interactions using
820 "netVisual_diffInteraction" and RankNet analysis "rankNet" to quantify differential signaling contributions.
821 Communication patterns were identified separately for outgoing and incoming signals using
822 "identifyCommunicationPatterns" based on unsupervised clustering of signaling probabilities. Heatmap was
823 generated using "netVisual_heatmap" function to show differential number of interactions and interaction
824 strength in the cell-cell communication network between two dietary conditions. For visualization of specific
825 pathways such as Desmosterol and Galectin, both the interaction networks were plotted using
826 "netVisual_aggregate". Ligand and receptor expressions of these two pathways were plotted after identifying
827 significant ligand-receptor pairs and extracting related genes using "extractEnrichedLR" function, and plotting

828 them using Seurat "VlnPlot" function for Desmosterol and Galectin signaling pathways, respectively. Increased or
829 decreased significant ligand-receptor pairs from one cell type to other cell type were plotted using
830 "netVisual_bubble" function by specifying the source cluster and target clusters.
831
832 **RNA Scope in situ hybridization**
833 Tissues that were fixed and paraffin embedded for histological confirmation of pregnancy were sectioned at 5 μm
834 and mounted onto glass slides. The chromogenic RNAscope 2.5 HD Duplex Assay (ACD Bio) was performed
835 according to manufacturer's instructions. The Mm-Unc13-C1 (ACD bio), Mm-Nos1-C1 (ACD bio), and Mm-Hand2-
836 C2 (ACD bio) probes were used. Slides were imaged with an AxioObserver inverted microscope (Zeiss) using the
837 5X, 20X, and 40X Plan-Apochromat/0.8NA objective (Zeiss). Quantification of *in situ* RNAScope signals were
838 performed using Qupath software [87]
839
840 **Interactive App Generation**
841 The ShinyCell R package[88] (v2.1.0) was used to assemble the "Mice Maternal Obesity" app and the rsconnect R
842 package (v1.4.1) was used to publish the app on the shinyapps.io server for public access.
843
844 **QUANTIFICATION AND STATISTICAL ANALYSIS**
845 **Statistical analysis**
846 All statistical analyses in this study were performed in R (v.4.4.2; https://www.R-project.org). One dam or
847 pregnancy was considered a biological replicate. The normality of all data sets was determined using the
848 D'Agostino-Pearson K2 test. Pairwise comparisons were made using univariate linear models with maternal diet
849 as the dependent variable, or Mann-Whitney U-test where the data were discrete values or non-normally
850 distributed. For time series experiments or those with repeated/replicate measures, linear mixed effects models
851 were constructed using the lmerTest package [89] (version 3.1-3, RRID SCR_015656) and analyzed using two-way
852 ANOVA with Type 3 sum of squares and Kenward-Roger calculated denominator degrees of freedom using the
853 Anova function in the car package (version 3.1-3, RRID SCR_022137). For these analyses, maternal diet and time
854 were set as fixed effects, and dam as a random effect for nesting repeated measurements. Where significant main
855 effects or interactions were present, pairwise post hoc comparisons were made between the estimated marginal
856 means using Tukey's HSD method with the emmeans package [90] (v.1.8.5, RRID SCR_018734). For all analyses, $p <$
857 0.05 was used as a nominal threshold for determining statistical significance. Please refer to the relevant scRNAseq
858 analysis methods for statistical analyses applied to single-cell datasets.
859

860 **EXCEL TABLE TITLES AND LEGENDS**

861 **Table S1:** Metadata, related to Methods, Figure 1 and Supplemental Figure 1
862 **Table S2:** Full list of gene markers, related to Supplemental Figure 1
863 **Table S3**: List of DEGs in E5.5 endometrial cell types as a consequence of obesogenic diet, related to Figure 2.
864 **Table S4:** List of enriched gene pathways in endometrial stromal cells, uNK, and Mϕ as a result of obesogenic
865 diet, related to Figure 2.
866 **Table S5:** Gene markers of *Hand2*$^{+}$ endometrial stromal cell subtypes, related to Methods, Figure 3, and
867 Supplemental Figure 3.
868 **Table S6:** List of DEGs in *Hand2*$^{+}$ endometrial stromal cell types as a consequence of obesogenic diet, related to
869 Figure 3 and Supplemental Figure 3.
870 **Table S7:** List of enriched gene pathways in Hand2+ endometrial stromal cells as a consequence of obesogenic
871 diet, related to Figure 3 and Supplemental Figure 3.
872 **Table S8:** CellChat rankNet signaling contribution results, related to Figure 5.
873
874

875 **REFERENCES**

876 1. Gellersen, B., and Brosens, J.J. (2014). Cyclic decidualization of the human endometrium in
877 reproductive health and failure. Endocr. Rev. *35*, 851–905. https://doi.org/10.1210/er.2014-1045.

878 2. Mosebarger, A., Vidal, M.S., Bento, G.F.C., Lintao, R.C.V., Severino, M.E.L., Kumar Kammala,
879 A., and Menon, R. (2024). Immune cells at the feto-maternal interface: Comprehensive
880 characterization and insights into term labor. J. Reprod. Immunol. *163*, 104239.
881 https://doi.org/10.1016/j.jri.2024.104239.

882 3. Ander, S.E., Diamond, M.S., and Coyne, C.B. (2019). Immune responses at the maternal-fetal
883 interface. Sci. Immunol. *4*, eaat6114. https://doi.org/10.1126/sciimmunol.aat6114.

884 4. Massri, N., Loia, R., Sones, J.L., Arora, R., and Douglas, N.C. (2023). Vascular changes in the
885 cycling and early pregnant uterus. JCI Insight *8*, e163422.
886 https://doi.org/10.1172/jci.insight.163422.

887 5. Fukui, Y., Hirota, Y., Matsuo, M., Gebril, M., Akaeda, S., Hiraoka, T., and Osuga, Y. (2019).
888 Uterine receptivity, embryo attachment, and embryo invasion: Multistep processes in embryo
889 implantation. Reprod. Med. Biol. *18*, 234–240. https://doi.org/10.1002/rmb2.12280.

890 6. Lucas, E.S., Vrljicak, P., Muter, J., Diniz-da-Costa, M.M., Brighton, P.J., Kong, C.-S., Lipecki, J.,
891 Fishwick, K.J., Odendaal, J., Ewington, L.J., et al. (2020). Recurrent pregnancy loss is associated
892 with a pro-senescent decidual response during the peri-implantation window. Commun. Biol. *3*, 37.
893 https://doi.org/10.1038/s42003-020-0763-1.

894 7. Tran, D.N., Hwang, Y.J., Kim, K.C., Li, R., Marquardt, R.M., Chen, C., Young, S.L., Lessey, B.A.,
895 Kim, T.H., Cheon, Y.-P., et al. (2025). GRB2 regulation of essential signaling pathways in the
896 endometrium is critical for implantation and decidualization. Nat. Commun. *16*, 2192.
897 https://doi.org/10.1038/s41467-025-57173-2.

898 8. Wang, H.-Q., Liu, Y., Li, D., Liu, J.-Y., Jiang, Y., He, Y., Zhou, J.-D., Wang, Z.-L., Tang, X.-Y.,
899 Zhang, Y., et al. (2023). Maternal and embryonic signals cause functional differentiation of luminal
900 epithelial cells and receptivity establishment. Dev. Cell *58*, 2376-2392.e6.
901 https://doi.org/10.1016/j.devcel.2023.08.004.

902 9. Garrido-Gómez, T., Castillo-Marco, N., Cordero, T., and Simón, C. (2022). Decidualization
903 resistance in the origin of preeclampsia. Am. J. Obstet. Gynecol. *226*, S886–S894.
904 https://doi.org/10.1016/j.ajog.2020.09.039.

905 10. Yang, J., Gong, L., Liu, Q., Zhao, H., Wang, Z., Li, X., Tian, W., and Zhou, Q. (2023). Single-cell
906 RNA-seq reveals developmental deficiencies in both the placentation and the decidualization in
907 women with late-onset preeclampsia. Front. Immunol. *14*, 1142273.
908 https://doi.org/10.3389/fimmu.2023.1142273.

909 11. Mori, M., Bogdan, A., Balassa, T., Csabai, T., and Szekeres-Bartho, J. (2016). The decidua-the
910 maternal bed embracing the embryo-maintains the pregnancy. Semin. Immunopathol. *38*, 635–649.
911 https://doi.org/10.1007/s00281-016-0574-0.

912 12. Li, R., Wang, T., Xu, X., Emery, O.M., Yi, M., Wu, S.-P., and DeMayo, F.J. (2022). Spatial
913 transcriptomic profiles of mouse uterine microenvironments at pregnancy day 7.5. Biol. Reprod.
914 *107*, 529–545. https://doi.org/10.1093/biolre/ioac061.

915 13. Woods, L., Perez-Garcia, V., Kieckbusch, J., Wang, X., DeMayo, F., Colucci, F., and Hemberger,
916 M. (2017). Decidualisation and placentation defects are a major cause of age-related reproductive
917 decline. Nat. Commun. *8*, 352. https://doi.org/10.1038/s41467-017-00308-x.

918 14. Yang, M., Ong, J., Meng, F., Zhang, F., Shen, H., Kitt, K., Liu, T., Tao, W., and Du, P. (2023).
919 Spatiotemporal insight into early pregnancy governed by immune-featured stromal cells. Cell *186*,
920 4271-4288.e24. https://doi.org/10.1016/j.cell.2023.08.020.

921 15. Greenbaum, S., Averbukh, I., Soon, E., Rizzuto, G., Baranski, A., Greenwald, N.F., Kagel, A.,
922 Bosse, M., Jaswa, E.G., Khair, Z., et al. (2023). A spatially resolved timeline of the human
923 maternal-fetal interface. Nature *619*, 595–605. https://doi.org/10.1038/s41586-023-06298-9.

924 16. De Assis, V., Kayisli, U.A., Ozmen, A., Semerci, N., Totary-Jain, H., Pakasticali, N., Halade, G.V.,
925 Lockwood, C.J., and Guzeloglu-Kayisli, O. (2024). Decidual Cells Block Inflammation-Mediated
926 Inhibition of 15-Hydroxyprostaglandin Dehydrogenase in Trophoblasts. Am. J. Pathol. *194*, 1724–
927 1736. https://doi.org/10.1016/j.ajpath.2024.05.005.

928 17. Kayisli, U.A., Korgun, E.T., Akkoyunlu, G., Arici, A., and Demir, R. (2005). Expression of
929 integrin α5 and integrin β4 and their extracellular ligands fibronectin and laminin in human decidua
930 during early pregnancy and its sex steroid-mediated regulation. Acta Histochem. *107*, 173–185.
931 https://doi.org/10.1016/j.acthis.2005.01.005.

932 18. Yu, J., Berga, S.L., Zou, W., and Taylor, R.N. (2019). Interleukin-1β inhibits estrogen receptor-α,
933 progesterone receptors A and B and biomarkers of human endometrial stromal cell differentiation:
934 implications for endometriosis. Mol. Hum. Reprod. *25*, 625–637.
935 https://doi.org/10.1093/molehr/gaz045.

936 19. Fang, X., Ni, N., Gao, Y., Lydon, J.P., Ivanov, I., Rijnkels, M., Bayless, K.J., and Li, Q. (2020).
937 Transforming growth factor beta signaling and decidual integrity in mice†. Biol. Reprod. *103*,
938 1186–1198. https://doi.org/10.1093/biolre/ioaa155.

939 20. Chen, J., Yin, T., Hu, X., Chang, L., Sang, Y., Xu, L., Zhao, W., Liu, L., Xu, C., Lin, Y., et al.
940 (2024). CD36-mediated arachidonic acid influx from decidual stromal cells increases inflammatory
941 macrophages in miscarriage. Cell Rep. *43*, 114881. https://doi.org/10.1016/j.celrep.2024.114881.

942 21. Jia, Z., Wei, Y., Zhang, Y., Song, K., and Yuan, J. (2024). Metabolic reprogramming and
943 heterogeneity during the decidualization process of endometrial stromal cells. Cell Commun.
944 Signal. *22*. https://doi.org/10.1186/s12964-024-01763-y.

945 22. Robertson, S.A., Moldenhauer, L.M., Green, E.S., Care, A.S., and Hull, M.L. (2022). Immune
946 determinants of endometrial receptivity: a biological perspective. Fertil. Steril. *117*, 1107–1120.
947 https://doi.org/10.1016/j.fertnstert.2022.04.023.

948 23. Venkatesh, S.S., Ferreira, T., Benonisdottir, S., Rahmioglu, N., Becker, C.M., Granne, I.,
949 Zondervan, K.T., Holmes, M.V., Lindgren, C.M., and Wittemans, L.B.L. (2022). Obesity and risk

950 of female reproductive conditions: A Mendelian randomisation study. PLoS Med. *19*, e1003679.
951 https://doi.org/10.1371/journal.pmed.1003679.

952 24. Practice Committee of the American Society for Reproductive Medicine. Electronic address:
953 asrm@asrm.org and Practice Committee of the American Society for Reproductive Medicine
954 (2021). Obesity and reproduction: a committee opinion. Fertil. Steril. *116*, 1266–1285.
955 https://doi.org/10.1016/j.fertnstert.2021.08.018.

956 25. Zhang, C.X.W., Candia, A.A., and Sferruzzi-Perri, A.N. (2024). Placental inflammation, oxidative
957 stress, and fetal outcomes in maternal obesity. Trends Endocrinol. Metab. TEM *35*, 638–647.
958 https://doi.org/10.1016/j.tem.2024.02.002.

959 26. Bellver, J., Melo, M.A.B., Bosch, E., Serra, V., Remohí, J., and Pellicer, A. (2007). Obesity and
960 poor reproductive outcome: the potential role of the endometrium. Fertil. Steril. *88*, 446–451.
961 https://doi.org/10.1016/j.fertnstert.2006.11.162.

962 27. Cozzolino, M., García-Velasco, J.A., Meseguer, M., Pellicer, A., and Bellver, J. (2021). Female
963 obesity increases the risk of miscarriage of euploid embryos. Fertil. Steril. *115*, 1495–1502.
964 https://doi.org/10.1016/j.fertnstert.2020.09.139.

965 28. Rhee, J.S., Saben, J.L., Mayer, A.L., Schulte, M.B., Asghar, Z., Stephens, C., Chi, M.M.-Y., and
966 Moley, K.H. (2016). Diet-induced obesity impairs endometrial stromal cell decidualization: a
967 potential role for impaired autophagy. Hum. Reprod. *31*, 1315–1326.
968 https://doi.org/10.1093/humrep/dew048.

969 29. Ray, J.G., Abdulaziz, K.E., Berger, H., and DOH-NET (Diabetes, Obesity, and Hypertension in
970 Pregnancy Research Network) (2022). Aspirin Use for Preeclampsia Prevention Among Women
971 With Prepregnancy Diabetes, Obesity, and Hypertension. JAMA *327*, 388–390.
972 https://doi.org/10.1001/jama.2021.22749.

973 30. Bellver, J., Marín, C., Lathi, R.B., Murugappan, G., Labarta, E., Vidal, C., Giles, J., Cabanillas, S.,
974 Marzal, A., Galliano, D., et al. (2021). Obesity Affects Endometrial Receptivity by Displacing the
975 Window of Implantation. Reprod. Sci. Thousand Oaks Calif *28*, 3171–3180.
976 https://doi.org/10.1007/s43032-021-00631-1.

977 31. Gohir, W., Kennedy, K.M., Wallace, J.G., Saoi, M., Bellissimo, C.J., Britz-McKibbin, P., Petrik,
978 J.J., Surette, M.G., and Sloboda, D.M. (2019). High-fat diet intake modulates maternal intestinal
979 adaptations to pregnancy and results in placental hypoxia, as well as altered fetal gut barrier
980 proteins and immune markers. J. Physiol. *597*, 3029–3051. https://doi.org/10.1113/JP277353.

981 32. Baltayeva, J., Konwar, C., Castellana, B., Mara, D.L., Christians, J.K., and Beristain, A.G. (2020).
982 Obesogenic diet exposure alters uterine natural killer cell biology and impairs vasculature
983 remodeling in mice†. Biol. Reprod. *102*, 63–75. https://doi.org/10.1093/biolre/ioz163.

984 33. Van Der Heijden, R.A., Sheedfar, F., Morrison, M.C., Hommelberg, P.P., Kor, D., Kloosterhuis,
985 N.J., Gruben, N., Youssef, S.A., De Bruin, A., Hofker, M.H., et al. (2015). High-fat diet induced
986 obesity primes inflammation in adipose tissue prior to liver in C57BL/6j mice. Aging *7*, 256–268.
987 https://doi.org/10.18632/aging.100738.

988 34. Öhman, M.K., Shen, Y., Obimba, C.I., Wright, A.P., Warnock, M., Lawrence, D.A., and Eitzman,
989 D.T. (2008). Visceral Adipose Tissue Inflammation Accelerates Atherosclerosis in Apolipoprotein
990 E–Deficient Mice. Circulation *117*, 798–805. https://doi.org/10.1161/circulationaha.107.717595.

991 35. Saatcioglu, H.D., Kano, M., Horn, H., Zhang, L., Samore, W., Nagykery, N., Meinsohn, M.-C.,
992 Hyun, M., Suliman, R., Poulo, J., et al. (2019). Single-cell sequencing of neonatal uterus reveals an
993 Misr2+ endometrial progenitor indispensable for fertility. eLife *8*, e46349.
994 https://doi.org/10.7554/eLife.46349.

995 36. He, J.-P., Tian, Q., Zhu, Q.-Y., and Liu, J.-L. (2022). Single-cell analysis of mouse uterus at the
996 invasion phase of embryo implantation. Cell Biosci. *12*, 13. https://doi.org/10.1186/s13578-022-
997 00749-y.

998 37. Hao, Y., Stuart, T., Kowalski, M.H., Choudhary, S., Hoffman, P., Hartman, A., Srivastava, A.,
999 Molla, G., Madad, S., Fernandez-Granda, C., et al. (2024). Dictionary learning for integrative,
1000 multimodal and scalable single-cell analysis. Nat. Biotechnol. *42*, 293–304.
1001 https://doi.org/10.1038/s41587-023-01767-y.

1002 38. Kanamori-Katayama, M., Kaiho, A., Ishizu, Y., Okamura-Oho, Y., Hino, O., Abe, M., Kishimoto,
1003 T., Sekihara, H., Nakamura, Y., Suzuki, H., et al. (2011). LRRN4 and UPK3B are markers of
1004 primary mesothelial cells. PloS One *6*, e25391. https://doi.org/10.1371/journal.pone.0025391.

1005 39. Filant, J., and Spencer, T.E. (2013). Cell-specific transcriptional profiling reveals candidate
1006 mechanisms regulating development and function of uterine epithelia in mice. Biol. Reprod. *89*, 86.
1007 https://doi.org/10.1095/biolreprod.113.111971.

1008 40. Sawano, A., Iwai, S., Sakurai, Y., Ito, M., Shitara, K., Nakahata, T., and Shibuya, M. (2001). Flt-1,
1009 vascular endothelial growth factor receptor 1, is a novel cell surface marker for the lineage of
1010 monocyte-macrophages in humans. Blood *97*, 785–791. https://doi.org/10.1182/blood.v97.3.785.

1011 41. Li, Q., Kannan, A., DeMayo, F.J., Lydon, J.P., Cooke, P.S., Yamagishi, H., Srivastava, D., Bagchi,
1012 M.K., and Bagchi, I.C. (2011). The antiproliferative action of progesterone in uterine epithelium is
1013 mediated by Hand2. Science *331*, 912–916. https://doi.org/10.1126/science.1197454.

1014 42. Oliveira, S.F., Abrahamsohn, P.A., Nagata, T., and Zorn, T.M. (1995). Incorporation of 3H-amino
1015 acids by endometrial stromal cells during decidualization in the mouse. A radioautographical study.
1016 Cell. Mol. Biol. Noisy--Gd. Fr. *41*, 107–116.

1017 43. Kiss, M.G., Papac-Miličević, N., Porsch, F., Tsiantoulas, D., Hendrikx, T., Takaoka, M., Dinh,
1018 H.Q., Narzt, M.-S., Göderle, L., Ozsvár-Kozma, M., et al. (2023). Cell-autonomous regulation of
1019 complement C3 by factor H limits macrophage efferocytosis and exacerbates atherosclerosis.
1020 Immunity *56*, 1809-1824.e10. https://doi.org/10.1016/j.immuni.2023.06.026.

1021 44. Barallobre-Barreiro, J., Radovits, T., Fava, M., Mayr, U., Lin, W.-Y., Ermolaeva, E., Martínez-
1022 López, D., Lindberg, E.L., Duregotti, E., Daróczi, L., et al. (2021). Extracellular Matrix in Heart
1023 Failure: Role of ADAMTS5 in Proteoglycan Remodeling. Circulation *144*, 2021–2034.
1024 https://doi.org/10.1161/CIRCULATIONAHA.121.055732.

1025 45. Sekulovski, N., Whorton, A.E., Shi, M., Hayashi, K., and MacLean, J.A. (2021). Insulin signaling
1026 is an essential regulator of endometrial proliferation and implantation in mice. FASEB J. Off. Publ.
1027 Fed. Am. Soc. Exp. Biol. *35*, e21440. https://doi.org/10.1096/fj.202002448R.

1028 46. Reese, J., Binart, N., Brown, N., Ma, W.G., Paria, B.C., Das, S.K., Kelly, P.A., and Dey, S.K.
1029 (2000). Implantation and decidualization defects in prolactin receptor (PRLR)-deficient mice are
1030 mediated by ovarian but not uterine PRLR. Endocrinology *141*, 1872–1881.
1031 https://doi.org/10.1210/endo.141.5.7464.

1032 47. Ma, S., Charron, J., and Erikson, R.L. (2003). Role of Plk2 (Snk) in mouse development and cell
1033 proliferation. Mol. Cell. Biol. *23*, 6936–6943. https://doi.org/10.1128/MCB.23.19.6936-6943.2003.

1034 48. Raza, H. (2011). Dual localization of glutathione S-transferase in the cytosol and mitochondria:
1035 implications in oxidative stress, toxicity and disease. FEBS J. *278*, 4243–4251.
1036 https://doi.org/10.1111/j.1742-4658.2011.08358.x.

1037 49. Bibby, J.A., Agarwal, D., Freiwald, T., Kunz, N., Merle, N.S., West, E.E., Singh, P., Larochelle,
1038 A., Chinian, F., Mukherjee, S., et al. (2022). Systematic single-cell pathway analysis to
1039 characterize early T cell activation. Cell Rep. *41*, 111697.
1040 https://doi.org/10.1016/j.celrep.2022.111697.

1041 50. Cerro, J.A., and Pintar, J.E. (1997). Insulin-like growth factor binding protein gene expression in
1042 the pregnant rat uterus and placenta. Dev. Biol. *184*, 278–295.
1043 https://doi.org/10.1006/dbio.1997.8533.

1044 51. Spencer, T.E., Lowke, M.T., Davenport, K.M., Dhakal, P., and Kelleher, A.M. (2023). Single-cell
1045 insights into epithelial morphogenesis in the neonatal mouse uterus. Proc. Natl. Acad. Sci. U. S. A.
1046 *120*, e2316410120. https://doi.org/10.1073/pnas.2316410120.

1047 52. Velmurugan, B.K., Yeh, K.-T., Hsieh, M.-J., Yeh, C.-M., Lin, C.-C., Kao, C.-Y., Huang, L.-R., and
1048 Lin, S.-H. (2019). UNC13C Suppress Tumor Progression via Inhibiting EMT Pathway and
1049 Improves Survival in Oral Squamous Cell Carcinoma. Front. Oncol. *9*, 728.
1050 https://doi.org/10.3389/fonc.2019.00728.

1051 53. Lee, K.Y., Jeong, J.-W., Wang, J., Ma, L., Martin, J.F., Tsai, S.Y., Lydon, J.P., and DeMayo, F.J.
1052 (2007). Bmp2 is critical for the murine uterine decidual response. Mol. Cell. Biol. *27*, 5468–5478.
1053 https://doi.org/10.1128/MCB.00342-07.

1054 54. Weng, L., Hübner, R., Claessens, A., Smits, P., Wauters, J., Tylzanowski, P., Van Marck, E., and
1055 Merregaert, J. (2003). Isolation and characterization of chondrolectin (Chodl), a novel C-type lectin
1056 predominantly expressed in muscle cells. Gene *308*, 21–29. https://doi.org/10.1016/s0378-
1057 1119(03)00425-6.

1058 55. Qiu, X., Hill, A., Packer, J., Lin, D., Ma, Y.-A., and Trapnell, C. (2017). Single-cell mRNA
1059 quantification and differential analysis with Census. Nat. Methods *14*, 309–315.
1060 https://doi.org/10.1038/nmeth.4150.

1061 56. Rawlings, T.M., Makwana, K., Taylor, D.M., Molè, M.A., Fishwick, K.J., Tryfonos, M., Odendaal,
1062 J., Hawkes, A., Zernicka-Goetz, M., Hartshorne, G.M., et al. (2021). Modelling the impact of

1063 decidual senescence on embryo implantation in human endometrial assembloids. eLife *10*, e69603.
1064 https://doi.org/10.7554/eLife.69603.

1065 57. Cao, J., Spielmann, M., Qiu, X., Huang, X., Ibrahim, D.M., Hill, A.J., Zhang, F., Mundlos, S.,
1066 Christiansen, L., Steemers, F.J., et al. (2019). The single-cell transcriptional landscape of
1067 mammalian organogenesis. Nature *566*, 496–502. https://doi.org/10.1038/s41586-019-0969-x.

1068 58. Street, K., Risso, D., Fletcher, R.B., Das, D., Ngai, J., Yosef, N., Purdom, E., and Dudoit, S.
1069 (2018). Slingshot: cell lineage and pseudotime inference for single-cell transcriptomics. BMC
1070 Genomics *19*, 477. https://doi.org/10.1186/s12864-018-4772-0.

1071 59. Jin, S., Plikus, M.V., and Nie, Q. (2025). CellChat for systematic analysis of cell–cell
1072 communication from single-cell transcriptomics. Nat. Protoc. *20*, 180–219.
1073 https://doi.org/10.1038/s41596-024-01045-4.

1074 60. Zhang, X., McDonald, J.G., Aryal, B., Canfrán-Duque, A., Goldberg, E.L., Araldi, E., Ding, W.,
1075 Fan, Y., Thompson, B.M., Singh, A.K., et al. (2021). Desmosterol suppresses macrophage
1076 inflammasome activation and protects against vascular inflammation and atherosclerosis. Proc.
1077 Natl. Acad. Sci. U. S. A. *118*, e2107682118. https://doi.org/10.1073/pnas.2107682118.

1078 61. Li, Y., Sang, Y., Chang, Y., Xu, C., Lin, Y., Zhang, Y., Chiu, P.C.N., Yeung, W.S.B., Zhou, H.,
1079 Dong, N., et al. (2024). A Galectin-9-Driven CD11chigh Decidual Macrophage Subset Suppresses
1080 Uterine Vascular Remodeling in Preeclampsia. Circulation *149*, 1670–1688.
1081 https://doi.org/10.1161/CIRCULATIONAHA.123.064391.

1082 62. Antoniotti, G.S., Coughlan, M., Salamonsen, L.A., and Evans, J. (2018). Obesity associated
1083 advanced glycation end products within the human uterine cavity adversely impact endometrial
1084 function and embryo implantation competence. Hum. Reprod. *33*, 654–665.
1085 https://doi.org/10.1093/humrep/dey029.

1086 63. Fabozzi, G., Cimadomo, D., Maggiulli, R., Vaiarelli, A., Badajoz, V., Aura, M., Canosa, S.,
1087 Bongioanni, F., Benini, F., Livi, C., et al. (2024). Association between oocyte donors' or
1088 recipients' body mass index and clinical outcomes after first single blastocyst transfers-the uterus is
1089 the most affected. Fertil. Steril. *121*, 281–290. https://doi.org/10.1016/j.fertnstert.2023.07.029.

1090 64. Bellver, J., Martínez-Conejero, J.A., Labarta, E., Alamá, P., Melo, M.A.B., Remohí, J., Pellicer, A.,
1091 and Horcajadas, J.A. (2011). Endometrial gene expression in the window of implantation is altered
1092 in obese women especially in association with polycystic ovary syndrome. Fertil. Steril. *95*, 2335-
1093 2341.e8. https://doi.org/10.1016/j.fertnstert.2011.03.021.

1094 65. Wilson, M.R., Skalski, H., Reske, J.J., Wegener, M., Adams, M., Hostetter, G., Hoffmann, H.M.,
1095 Bernard, J.J., Bae-Jump, V.L., Teixeira, J.M., et al. (2022). Obesity alters the mouse endometrial
1096 transcriptome in a cell context-dependent manner. Reprod. Biol. Endocrinol. *20*.
1097 https://doi.org/10.1186/s12958-022-01030-0.

1098 66. Yuan, J., Aikawa, S., Deng, W., Bartos, A., Walz, G., Grahammer, F., Huber, T.B., Sun, X., and
1099 Dey, S.K. (2019). Primary decidual zone formation requires Scribble for pregnancy success in
1100 mice. Nat. Commun. *10*, 5425. https://doi.org/10.1038/s41467-019-13489-4.

1101 67. Huyen, D.V., and Bany, B.M. (2011). Evidence for a conserved function of heart and neural crest
1102 derivatives expressed transcript 2 in mouse and human decidualization. REPRODUCTION *142*,
1103 353–368. https://doi.org/10.1530/rep-11-0060.

1104 68. Li, Y., Dewar, A., Kim, Y.S., Dey, S.K., and Sun, X. (2020). Pregnancy success in mice requires
1105 appropriate cannabinoid receptor signaling for primary decidua formation. eLife *9*.
1106 https://doi.org/10.7554/elife.61762.

1107 69. Yang, R., Sun, L., Li, C.-F., Wang, Y.-H., Yao, J., Li, H., Yan, M., Chang, W.-C., Hsu, J.-M., Cha,
1108 J.-H., et al. (2021). Galectin-9 interacts with PD-1 and TIM-3 to regulate T cell death and is a
1109 target for cancer immunotherapy. Nat. Commun. *12*, 832. https://doi.org/10.1038/s41467-021-
1110 21099-2.

1111 70. Li, J., Liu, X.-G., Ge, R.-L., Yin, Y.-P., Liu, Y., Lu, W.-P., Huang, M., He, X.-Y., Wang, J., Cai,
1112 G., et al. (2023). The ligation between ERMAP, galectin-9 and dectin-2 promotes Kupffer cell
1113 phagocytosis and antitumor immunity. Nat. Immunol. *24*, 1813–1824.
1114 https://doi.org/10.1038/s41590-023-01634-7.

1115 71. Bermejo-Alvarez, P., Rosenfeld, C.S., and Roberts, R.M. (2012). Effect of maternal obesity on
1116 estrous cyclicity, embryo development and blastocyst gene expression in a mouse model. Hum.
1117 Reprod. *27*, 3513–3522. https://doi.org/10.1093/humrep/des327.

1118 72. Bellissimo, C.J., Ribeiro, T.A., Yeo, E., Jazwiec, P.A., Luo, H., Bains, J., Bowdish, D.M.E., and
1119 Sloboda, D.M. (2025). Maternal high-fat, high-sucrose diet-induced excess adiposity is linked to
1120 placental hypoxia and disruption of fetoplacental immune homeostasis in late gestation. Biol.
1121 Reprod., ioaf143. https://doi.org/10.1093/biolre/ioaf143.

1122 73. Baltayeva, J., Konwar, C., Castellana, B., Mara, D.L., Christians, J.K., and Beristain, A.G. (2019).
1123 Obesogenic diet exposure alters uterine natural killer cell biology and impairs vasculature
1124 remodeling in mice†. Biol. Reprod., ioz163. https://doi.org/10.1093/biolre/ioz163.

1125 74. Trapnell, C., Cacchiarelli, D., Grimsby, J., Pokharel, P., Li, S., Morse, M., Lennon, N.J., Livak,
1126 K.J., Mikkelsen, T.S., and Rinn, J.L. (2014). The dynamics and regulators of cell fate decisions are
1127 revealed by pseudotemporal ordering of single cells. Nat. Biotechnol. *32*, 381–386.
1128 https://doi.org/10.1038/nbt.2859.

1129 75. Qiu, X., Mao, Q., Tang, Y., Wang, L., Chawla, R., Pliner, H.A., and Trapnell, C. (2017). Reversed
1130 graph embedding resolves complex single-cell trajectories. Nat. Methods *14*, 979–982.
1131 https://doi.org/10.1038/nmeth.4402.

1132 76. Hayes, E.K., Lechowicz, A., Petrik, J.J., Storozhuk, Y., Paez-Parent, S., Dai, Q., Samjoo, I.A.,
1133 Mansell, M., Gruslin, A., Holloway, A.C., et al. (2012). Adverse Fetal and Neonatal Outcomes
1134 Associated with a Life-Long High Fat Diet: Role of Altered Development of the Placental
1135 Vasculature. PLOS ONE *7*, e33370. https://doi.org/10.1371/journal.pone.0033370.

1136 77. Germain, P.-L., Lun, A., Meixide, C.G., Macnair, W., and Robinson, M.D. (2022). Doublet
1137 identification in single-cell sequencing data using *scDblFinder*. Preprint at F1000Research,
1138 https://doi.org/10.12688/f1000research.73600.2 https://doi.org/10.12688/f1000research.73600.2.

1139 78. Hafemeister, C., and Satija, R. (2019). Normalization and variance stabilization of single-cell
1140 RNA-seq data using regularized negative binomial regression. Genome Biol. *20*, 296.
1141 https://doi.org/10.1186/s13059-019-1874-1.

1142 79. Finak, G., McDavid, A., Yajima, M., Deng, J., Gersuk, V., Shalek, A.K., Slichter, C.K., Miller,
1143 H.W., McElrath, M.J., Prlic, M., et al. (2015). MAST: a flexible statistical framework for assessing
1144 transcriptional changes and characterizing heterogeneity in single-cell RNA sequencing data.
1145 Genome Biol. *16*, 278. https://doi.org/10.1186/s13059-015-0844-5.

1146 80. Wickham, H. (2016). ggplot2 (Springer International Publishing) https://doi.org/10.1007/978-3-
1147 319-24277-4.

1148 81. Bibby, J.A., Agarwal, D., Freiwald, T., Kunz, N., Merle, N.S., West, E.E., Singh, P., Larochelle,
1149 A., Chinian, F., Mukherjee, S., et al. (2022). Systematic single-cell pathway analysis to
1150 characterize early T cell activation. Cell Rep. *41*. https://doi.org/10.1016/j.celrep.2022.111697.

1151 82. Subramanian, A., Tamayo, P., Mootha, V.K., Mukherjee, S., Ebert, B.L., Gillette, M.A., Paulovich,
1152 A., Pomeroy, S.L., Golub, T.R., Lander, E.S., et al. (2005). Gene set enrichment analysis: A
1153 knowledge-based approach for interpreting genome-wide expression profiles. Proc. Natl. Acad.
1154 Sci. *102*, 15545–15550. https://doi.org/10.1073/pnas.0506580102.

1155 83. Castanza, A.S., Recla, J.M., Eby, D., Thorvaldsdóttir, H., Bult, C.J., and Mesirov, J.P. (2023).
1156 Extending support for mouse data in the Molecular Signatures Database (MSigDB). Nat. Methods
1157 *20*, 1619–1620. https://doi.org/10.1038/s41592-023-02014-7.

1158 84. Gu, Z., Eils, R., and Schlesner, M. (2016). Complex heatmaps reveal patterns and correlations in
1159 multidimensional genomic data. Bioinformatics *32*, 2847–2849.
1160 https://doi.org/10.1093/bioinformatics/btw313.

1161 85. Qiu, X., Mao, Q., Tang, Y., Wang, L., Chawla, R., Pliner, H.A., and Trapnell, C. (2017). Reversed
1162 graph embedding resolves complex single-cell trajectories. Nat. Methods *14*, 979–982.
1163 https://doi.org/10.1038/nmeth.4402.

1164 86. Cao, J., Spielmann, M., Qiu, X., Huang, X., Ibrahim, D.M., Hill, A.J., Zhang, F., Mundlos, S.,
1165 Christiansen, L., Steemers, F.J., et al. (2019). The single-cell transcriptional landscape of
1166 mammalian organogenesis. Nature *566*, 496–502. https://doi.org/10.1038/s41586-019-0969-x.

1167 87. Bankhead, P., Loughrey, M.B., Fernández, J.A., Dombrowski, Y., McArt, D.G., Dunne, P.D.,
1168 McQuaid, S., Gray, R.T., Murray, L.J., Coleman, H.G., et al. (2017). QuPath: Open source
1169 software for digital pathology image analysis. Sci. Rep. *7*, 16878. https://doi.org/10.1038/s41598-
1170 017-17204-5.

1171 88. Ouyang, J.F., Kamaraj, U.S., Cao, E.Y., and Rackham, O.J.L. (2021). ShinyCell: simple and
1172 sharable visualization of single-cell gene expression data. Bioinformatics *37*, 3374–3376.
1173 https://doi.org/10.1093/bioinformatics/btab209.

1174 89. Kuznetsova, A., Brockhoff, P.B., and Christensen, R.H.B. (2017). **lmerTest** Package: Tests in
1175 Linear Mixed Effects Models. J. Stat. Softw. *82*. https://doi.org/10.18637/jss.v082.i13.

90. Searle, S.R., Speed, F.M., and Milliken, G.A. (1980). Population Marginal Means in the Linear Model: An Alternative to Least Squares Means. Am. Stat. *34*, 216–221. https://doi.org/10.1080/00031305.1980.10483031.